Investigation of $K^+\Lambda(1405)$ photoproduction at the BGOOD experiment

Linus Milorewin Plagens

Masterarbeit in Physik
angefertigt im Physikalischen Institut

vorgelegt der
Mathematisch-Naturwissenschaftlichen Fakultät
der
Rheinischen Friedrich-Wilhelms-Universität
Bonn

July 2024

I hereby declare that this thesis was formulated by myself and that no sources or tools other than those cited were used.

Paris, ...
Date Signature

1. Supervisor: Prof. Dr. Hartmut Schmieden
2. Supervisor: Prof. Dr. Reinhard Beck

Acknowledgements

I am deeply grateful to Prof. Schmieden for the opportunity to write my Master's thesis in his working group, for proposing such a captivating and unique topic that deepened my passion for research, and for the continuous support throughout the work. An additional thank you to Prof. Schmieden and Tom Jude for making it possible for me to participate in the meetings mostly remotely.

My gratitude also goes to Tom and Katrin who always showed generosity in sharing their expertise and time to help me with my analysis, amid their own demanding schedules. I am also indebted to Katrin for meticulously proofreading my thesis.

Moreover, I want to express my sincere thanks to all the group members for answering my questions and contributing to the wonderful experience I had during this period.

Last but not least, I would like to thank my family, my friends and Raphaël who supported me emotionally.

Contents

1 Introduction **1**
- 1.1 The Standard Model of particle physics . . . 1
- 1.2 Hadrons and quarks . . . 2

2 Research status of Λ(1405) **3**
- 2.1 The Λ(1405) resonance . . . 3
- 2.2 Line shape measurement at Jefferson Lab . . . 4
- 2.3 $K^+\Lambda(1405)$ photoproduction at BGOOD . . . 6

3 The BGOOD experiment at ELSA in Bonn **9**
- 3.1 The Electron Stretcher Accelerator (ELSA) . . . 9
- 3.2 The BGOOD detector . . . 10
  - 3.2.1 Tagging system . . . 10
  - 3.2.2 Central detector . . . 11
  - 3.2.3 Intermediate detectors . . . 12
  - 3.2.4 Forward spectrometer . . . 13
  - 3.2.5 Photon flux monitor . . . 14

4 Reconstruction of $\gamma p \to K^+\Lambda(1405)$ **15**
- 4.1 Software . . . 16
- 4.2 Particle identification . . . 16
  - 4.2.1 Identification of the K^+ . . . 16
  - 4.2.2 Identification of the π^0 . . . 17
  - 4.2.3 Identification of the p and of the π^- . . . 18
  - 4.2.4 Σ^+ selection . . . 21

5 Extraction of the yield **23**
- 5.1 RooFit method . . . 25
- 5.2 Sideband method . . . 25
- 5.3 Yield . . . 26

6 Determination of the differential cross section **29**
- 6.1 Target area density and solid angle . . . 29
- 6.2 Detection efficiency . . . 30
- 6.3 Differential cross section for $\gamma p \to K^+\Sigma^+\pi^-$ . . . 30
- 6.4 Contribution of Σ(1385) . . . 31
- 6.5 Systematic uncertainty estimation . . . 34
  - 6.5.1 Results for $\gamma p \to K^+\Lambda(1405)$ . . . 36

7 Summary and outlook 39

A Fits made with RooFit 41

B Plots from the Sideband method 43

C Differential cross section for $\gamma p \to K^+\Sigma(1385)$ 45

D Cross section for $\gamma p \to K^+\Sigma^+\pi^-$ 47

Bibliography 49

List of Figures 51

List of Tables 55

CHAPTER 1

Introduction

Particle physics is a big research field that was developed over the last century, when many individual particles have been discovered and their interactions studied. Questions arose about how our known matter is built up, which led to the elaboration of theories and models. The most successful one is the Standard Model of particle physics.

1.1 The Standard Model of particle physics

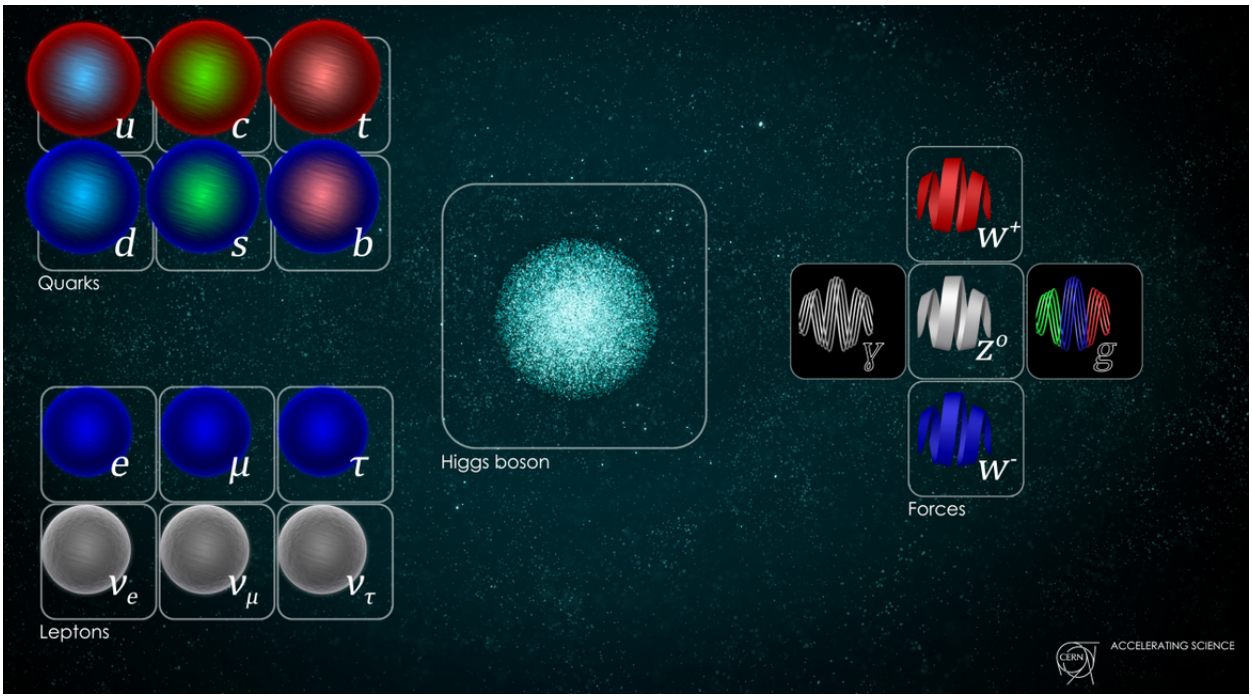

Figure 1.1: The Standard Model of particle physics: subatomic particles [1].

The Standard Model provides a classification of subatomic particles and describes their fundamental interactions as we understand them today. These are the three fundamental forces – the electromagnetic force, the weak force and the strong force. Gravitation is not included. The final development of the

Standard Model as we know it today took place in the 1970s [2].

Fig. 1.1 shows the elementary quarks and leptons, which form our matter, on the left, and the force-carrying particles, the exchange bosons of the fundamental forces, on the right. The quarks and leptons, that belong to the fermions, possess a half-integer spin. Quarks have six different flavors: up, down, charm, strange, top and bottom. The leptons are the electron, muon, tauon, and their corresponding neutrinos. These elementary fermions are organized in sets of pairs called "generations". Particles from the first generation are stable and have the smallest mass, whereas the other two generations are heavier and unstable. The bosons, shown on the right, have integer spins. They include the Higgs boson, the W and Z bosons, the gluon and the photon. The Higgs boson was only observed in 2012, which was a confirmation to its theoretical prediction [2, 3].

1.2 Hadrons and quarks

Over time, a great number of different particles was discovered and it was evident that they could not all be elementary. The physicists Gell-Mann and Zweig both had the thought that they must be composite particles with quarks being their constituents. In the conventional quark model, quarks form either particles consisting of 3 quarks, called baryons, or mesons, which are made up of a quark and an antiquark. A baryon which contains at least one strange or anti-strange quark is referred to as a "hyperon". These composite particles are collectively known as hadrons.

Quarks are held together within hadrons by the strong force, which is mediated by gluons. The theory that describes the strong interaction between quarks and gluons is called quantum chromodynamics (QCD). Apart from *electric charge*, quarks also carry *color charge*, which is the analog of electric charge in quantum electrodynamics (QED). Unlike photons, that do not carry an electric charge, gluons possess color charge. Three bound quarks each have one of the colors red, green, and blue, while a quark-antiquark pair has one of these colors and the corresponding anti-color. A composite object is always "white". Only such color neutral particles can exist freely. This means that quarks cannot be found alone or in other words, they are *confined*. This color confinement is the consequence of the constant force between the quarks. From the force follows an enormous, infinite energy requirement to separate quarks. Attempting to do so can lead to the creation of new pairs if enough energy is supplied, thus confinement is maintained.

The outline of this thesis is as follows: First, the current research status of the $\Lambda(1405)$ will be presented in Chapter 2. Then, Chapter 3 provides a description of the setup of the BGOOD experiment. Subsequently, Chapter 4 discusses the reconstruction of the $\Lambda(1405)$. In Chapter 5, the extraction of the yield is described. The determination of the differential cross section is presented in Chapter 6. Finally, Chapter 7 provides a summary and an outlook.

CHAPTER 2

Research status of Λ(1405)

2.1 The Λ(1405) resonance

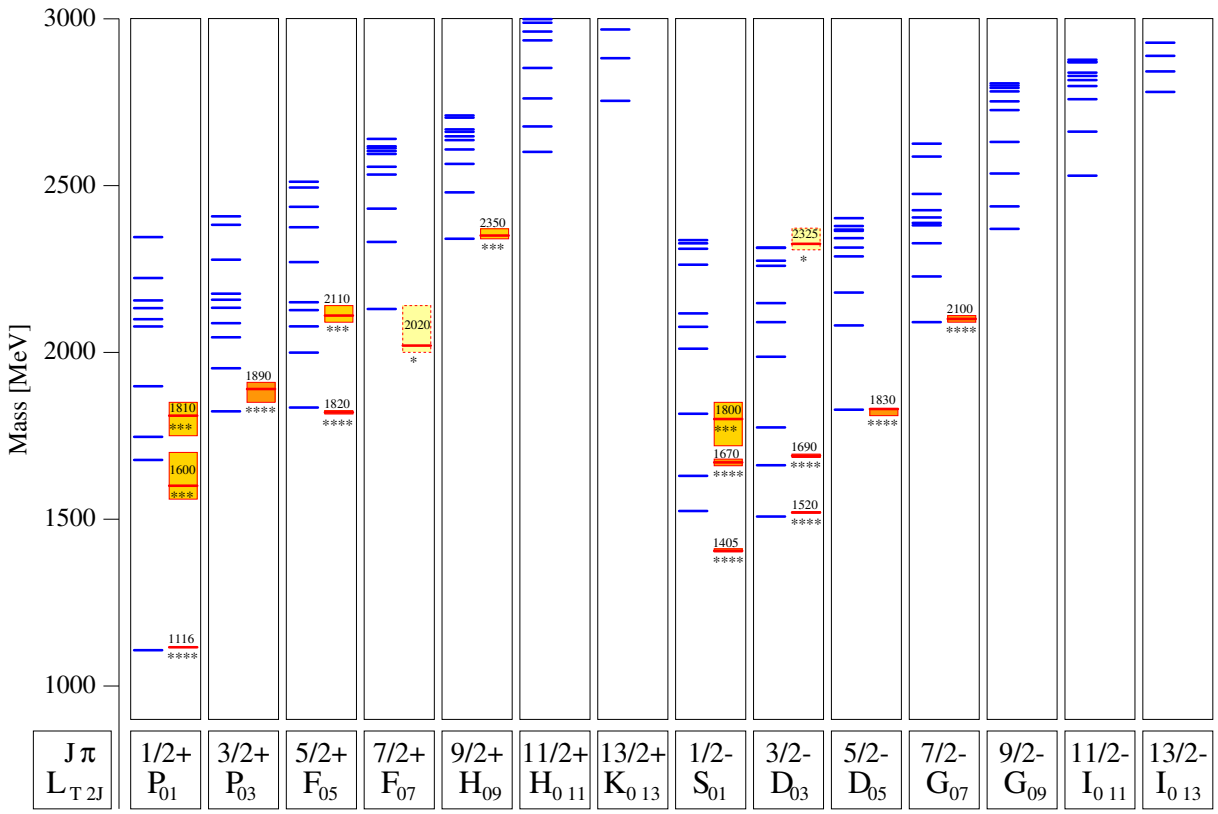

Figure 2.1: The calculated positive and negative parity Λ-resonance spectrum. The quantum numbers of the resonances are displayed on the x-axis, alongside their masses on the y-axis. The blue lines show the predicted states by theory, while the red lines indicate the measured states with their uncertainties delineated by yellow boxes [4].

Like atoms, hadrons can be excited to resonant states. These excited states decay by emitting mesons.

By investigating the decay, one can learn about the excited resonant state. The Λ(1405) is a resonance that can be created via meson photoproduction through the following reaction: $\gamma p \rightarrow K^{+}\Lambda(1405)$. It decays consequently into $(\Sigma\pi)^{0}$.

Figure 2.1 depicts various Λ^{*} resonances. The blue lines indicate the predicted states by theory, while the red lines are the experimentally determined resonances with their corresponding uncertainties displayed by the yellow boxes. These results are grouped by the total spin J and parity π. In addition, the angular momentum L is given. As it can be seen, there are plenty of *missing resonances*, i.e., states that were predicted by quark models, but have not been experimentally observed yet [5]. This problem remains unsolved until today. The resonance of interest, Λ(1405), is shown in the lower middle of the diagram, classified by $J^{\pi} = \frac{1}{2}^{-}$. As it contains one strange quark, it belongs to the hyperons. The $N^{*}(1535)$ state has also negative parity but no strange quark. This means, that its mass should be smaller than the mass of the Λ(1405), since strange quarks are remarkably heavier than up and down quarks. Nevertheless, the $N^{*}(1535)$ resonance has a higher mass than the Λ(1405) [4, 6].

In order to find a solution for this problem, models with multiquark states were developed. An example for a multiquark state is the today so-called tetraquark, that consists of two quark-antiquark pairs. It can be described as a meson-meson system. Pentaquarks have four quarks and one antiquark, which makes of them a molecular-like meson-baryon system. An illustration of such a hadronic molecule is shown in Fig. 2.2. These multiquark states are not included in the conventional quark model, but are possible in QCD [7, 8, 9].

As early as 1960, a long time before the establishment of the quark model, Dalitz and Tuan predicted the Λ(1405) resonance to be of a molecular nature [10, 11]. Rather than a three-quark state with the quarks up, down and strange, it would be an antikaon-nucleon molecule [12]. However, the precise nature of this enigmatic particle remained a subject of debate until more recent years. Only in 2016, the PDG stated: “It is the archetype of what is called a dynamically generated resonance, as pioneered by Dalitz and Tuan” [13].

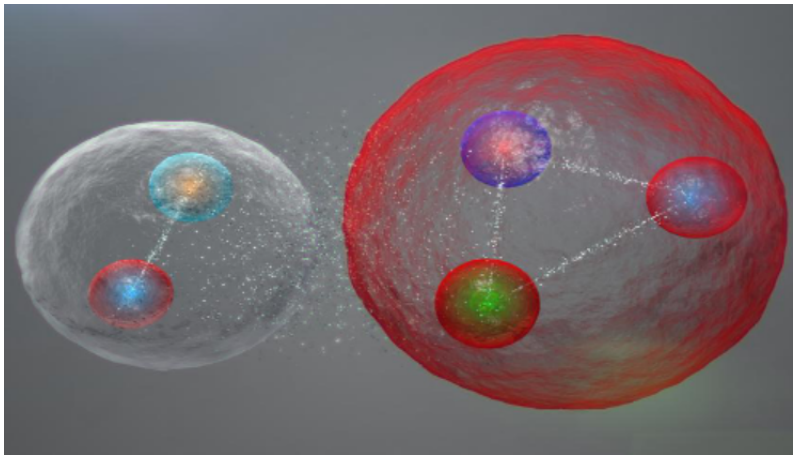

Figure 2.2: A pentaquark shown as a hadronic molecule of a meson and a baryon [1].

2.2 Line shape measurement at Jefferson Lab

Measurements of the line shapes, i.e., the invariant mass distributions of the different decay channels, have shown that these cannot be described by a simple Breit-Wigner distribution [14]. This was one of the evidences that the Λ(1405) must be a dynamically generated resonance [14]. It can be explained by

the fact that the cross section for the production of the $\Lambda(1405)$ is smaller above the $\bar{K}N$ threshold [15]. In order to better understand the dynamics that are present in the $\Lambda(1405)$, more precise measurements of the invariant mass distributions were made by the CLAS Collaboration in 2013 at Jefferson Lab [16]. The results are shown in Fig. 2.3 for a center-of-mass energy of $W = 2.1$ GeV. The $(\Sigma\pi)^0$ and $\bar{K}N$ thresholds as well as the $\Lambda(1405)$ mass are indicated by the vertical dashed lines. The $\Lambda(1405)$ lies over the $\Sigma\pi$ threshold and directly below the $N\bar{K}$ threshold. What can be seen is that the mass distributions differ for the three $\Sigma\pi$ final states. This is due to the fact that the neutral final state is purely isospin 0, while the two charged states are a mixture of isospin 1 and isospin 0 [16]. Moreover, the $\Lambda(1405)$ has a double-pole structure, where the two poles couple differently to the decay channels [17, 18]. The theoretical study of these phenomena is grounded in the chiral perturbation theory, which describes the dynamics of mesons and baryons in the low-energy region of quantum chromodynamics. [17, 18, 19].

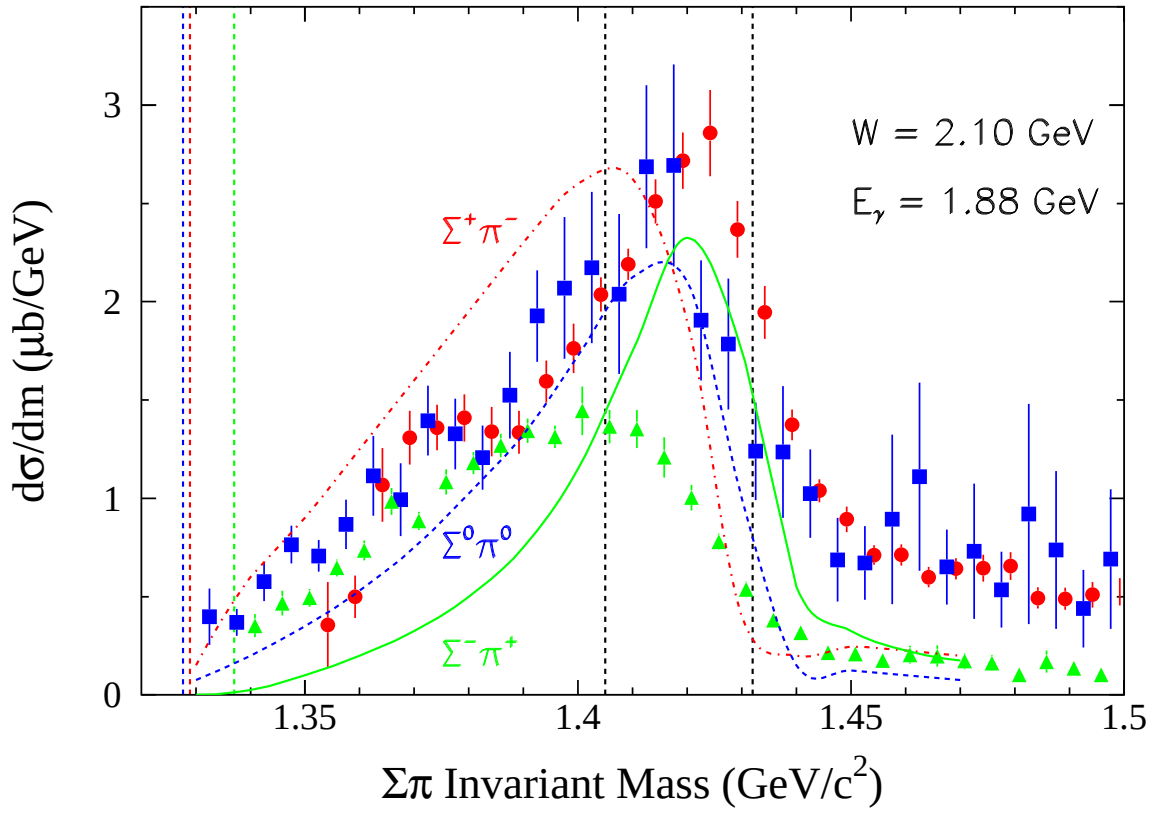

Figure 2.3: Invariant mass distributions (or line shapes) of the final states, $(\Sigma\pi)^0$, of the $\Lambda(1405)$ photoproduction. The $(\Sigma\pi)^0$ and $\bar{K}N$ thresholds as well as the $\Lambda(1405)$ mass are marked by the vertical dashed lines. The results were obtained by the CLAS Collaboration [16].

In addition to the line shape measurements, the differential cross section for $\gamma p \to K^+\Lambda(1405)$ has been measured by the CLAS Collaboration [20]. Measuring the differential photoproduction cross section can also reveal more about the nature of the $\Lambda(1405)$. This measurement contributed to the

improvement of theoretical models that study the production and the structure of the Λ(1405). However, their experimental setup at Jefferson Lab is not designed to reach very forward angles. Besides, the energy range of the cross section results is not in the vicinity of the $\bar{K}N$ threshold. Further experiments, and with more statistics, are necessary to study the Λ(1405).

2.3 $K^+\Lambda(1405)$ photoproduction at BGOOD

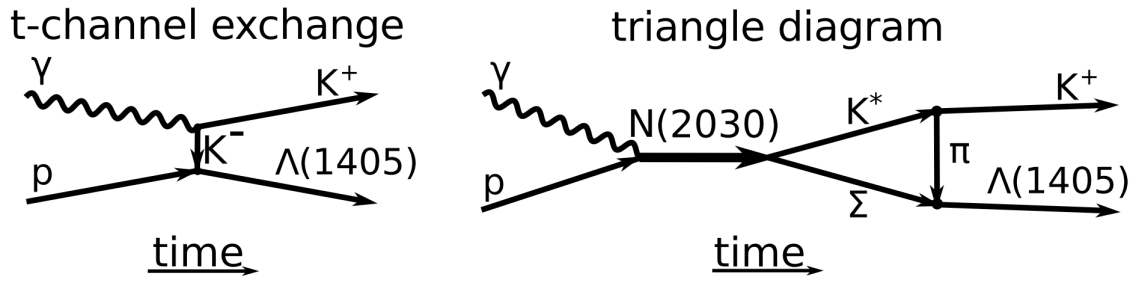

Figure 2.4: Two processes of Λ(1405) photoproduction [21].

Since the measurement from the CLAS Collaboration did not extend to very forward angles, $\cos\theta^{K^+}_{\mathrm{CM}} > 0.9$, additional measurements must be performed with very forward going particles. A measurement of the photoproduction Λ(1405) via the reaction $\gamma p \rightarrow K^+\Lambda(1405)$ was made at extremely forward angles at the BGOOD experiment [15, 21]. Kaons that propagate in forward direction have a high momentum. This means a low momentum transfers to the system. The Λ(1405) decays almost at rest. Therefore, forward-going kaons are essential for this experiment, since the probability to generate a bound state becomes higher.

This measurement put a focus on the neutral decay channel $\Lambda(1405) \rightarrow \Sigma^0\pi^0$. The neutral channel was chosen because there is no contribution from the Σ(1385). The mass of the Σ(1385) resonance is very close to the one of the Λ(1405) and it also decays into $\Sigma^+\pi^-$ and into $\Sigma^-\pi^+$, so that measuring the charged decay channels of the Λ(1405) would include a contribution from Σ(1385). In contrast, the neutral channel of the Σ(1385) is forbidden due to isospin symmetry. The total cross section for $\gamma p \rightarrow K^+\Lambda(1405)$ was determined and is shown in Fig. 2.5. The black squares mark the results of the BGOOD measurement and indicate a cusp-like structure. It can be described with a triangle singularity [22]. This is a phenomenon that occurs in specific Feynman diagrams that are called "triangle diagrams". It is represented in the right, in Fig. 2.4. The $N(2030)$ resonance drives the production of the Λ(1405) by first producing a K^* meson and a Σ baryon. The K^* subsequently decays into a K^+ and a pion. Next, the pion merges with the Σ to generate the Λ(1405). In the left, the t-channel exchange diagram is depicted, which is another possible process.

The BGOOD data shows good agreement with the data from the CLAS Collaboration [20], which is represented by red circles in Fig. 2.5. Additionally, the BGOOD data features finer binning and higher statistics.

In this thesis, I aim to determine the differential photoproduction cross section for $\gamma p \rightarrow K^+\Lambda(1405)$ in the region of very forward angles and for center-of-mass energies toward the $\bar{K}N$ threshold. Since the neutral channel, $\Lambda(1405) \rightarrow \Sigma^0\pi^0$, has already been measured [15][21], the next step is to investigate the charged channel, $\Lambda(1405) \rightarrow \Sigma^+\pi^-$.

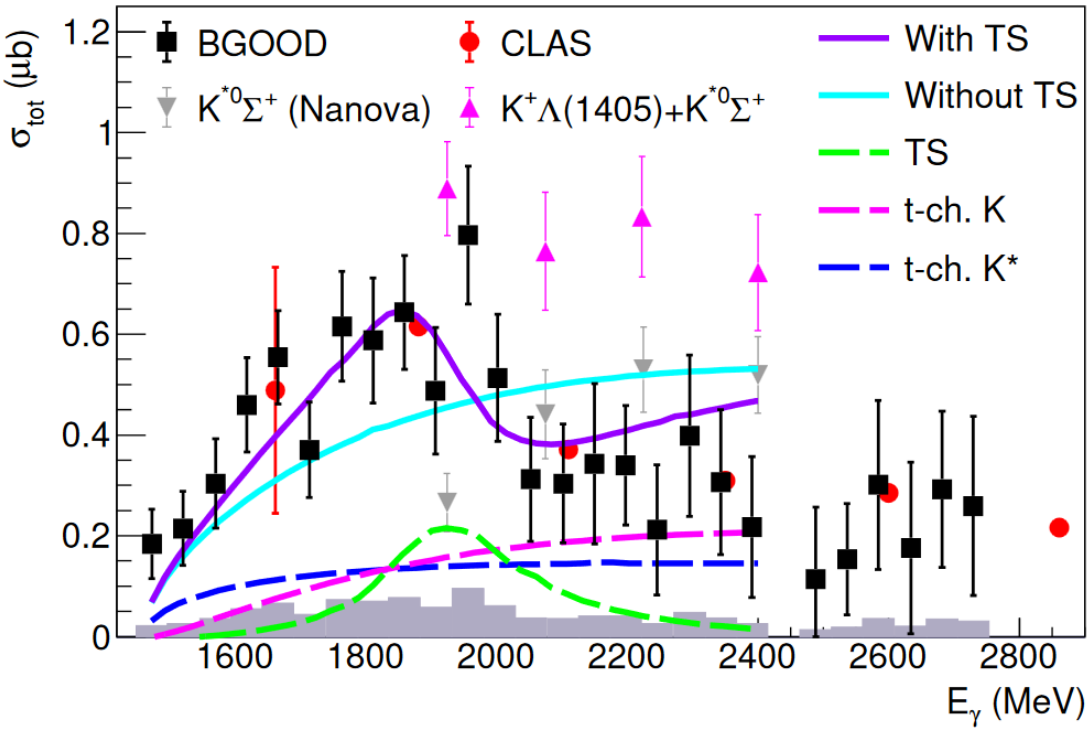

Figure 2.5: Total cross section for $\gamma p \rightarrow K^+\Lambda(1405)$ [21]. The black squares are the BGOOD data, the red circles are the data from the CLAS Collaboration. The systematic uncertainties are shown by the grey bars on the abscissa. The curves are the results of the model of Wang et al. [22].

CHAPTER 3

The BGOOD experiment at ELSA in Bonn

The BGOOD experiment at the Electron Stretcher Accelerator (ELSA) in Bonn is ideally suited to investigate $K^+\Lambda(1405)$ photoproduction. It combines almost 4π coverage for charged and neutral particles together with excellent particle identification in forward direction. In this chapter, the accelerator facility is introduced (Sec. 3.1) and the detector components are explained (Sec. 3.2).

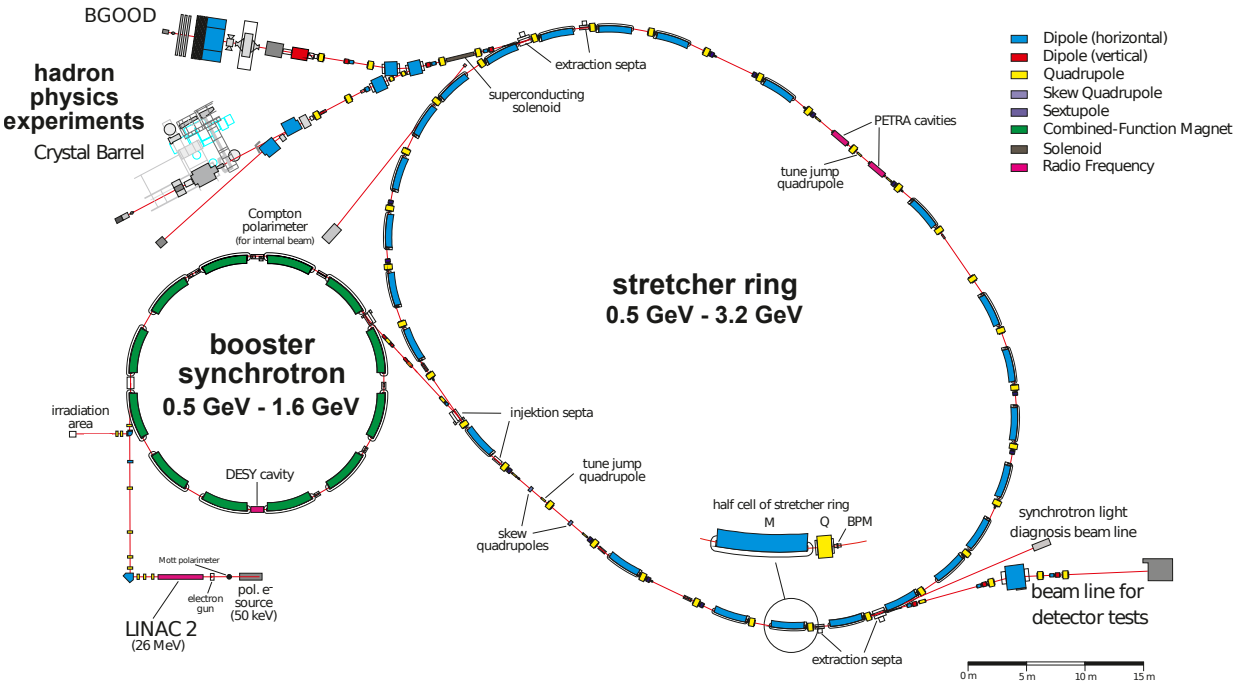

Figure 3.1: The Electrom Stretcher Accelerator (ELSA) facility with the LINAC 2, the booster synchrotron, the stretcher ring and the experiments [23].

3.1 The Electron Stretcher Accelerator (ELSA)

The Electron Stretcher Accelerator is a 3-stage accelerator with the injector LINAC, the booster synchrotron and the stretcher ring. Both, polarized and unpolarized electrons can be accelerated up to 3.2 GeV and are then ejected into the setups for the different experiments.

The electrons coming from a thermionic electron gun enter the LINAC 2 where they undergo an acceleration up to a maximum energy of 26 MeV. Subsequently, they are directed toward the booster synchrotron. Energies up to 1.6 GeV can be achieved before the electrons are transferred to the stretcher ring. This is repeated until the stretcher ring is filled. The electrons are then accelerated up to 3.2 GeV. In the end, the electrons are extracted to one of the experiments or to a designated area for detector testing [24, 25].

3.2 The BGOOD detector

The BGOOD[1] detector is located at the ELSA electron accelerator facility. The setup is well-suited for investigating both non-strange and strange meson photoproduction, with a focus on production thresholds and t-channel processes at low momentum transfer aligning with mesons at very forward angles. The integration of a BGO crystal calorimeter with 4π acceptance, and a forward large-aperture magnetic spectrometer, using an open dipole magnet, enables precise detection of neutral and charged particles [23]. These two principal components are depicted in Fig. 3.2 along with the remaining elements that are described in the subsequent sections. An electron beam is provided by ELSA.

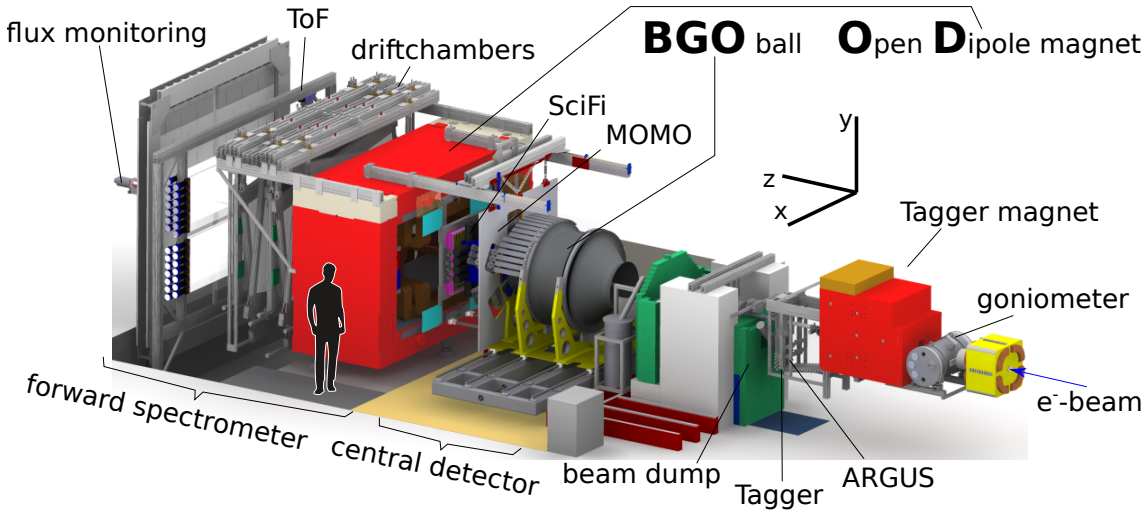

Figure 3.2: Overview of the BGOOD experiment showing the different components of the detector [23].

3.2.1 Tagging system

The electron beam from ELSA needs to be converted into a photon beam. It impinges on a radiator, as demonstrated in Fig. 3.3. This radiator can either be a diamond for a polarized photon beam, or a copper foil for unpolarized photons. The photon beam is generated via bremsstrahlung processes and continues straight ahead passing a dipole magnet which is placed directly after the radiator. The bremsstrahlung electrons are deflected by the magnetic field depending on their momenta, which is shown by the red trajectories in Fig. 3.3. A hodoscope then determines the position of these electrons using scintillators, so that their energy can be calculated. The energy of the photons is equal to the initial beam energy, E_0, reduced by the energy of the electrons after the bremsstrahlung process. Not only the energy is allocated to the corresponding photons but also the production time. Thus, a correlation to the hadronic reactions can be established. The remaining electrons are stopped in the beam dump [23, 26].

[1] **BGO** ball **O**pen **D**ipole magnet

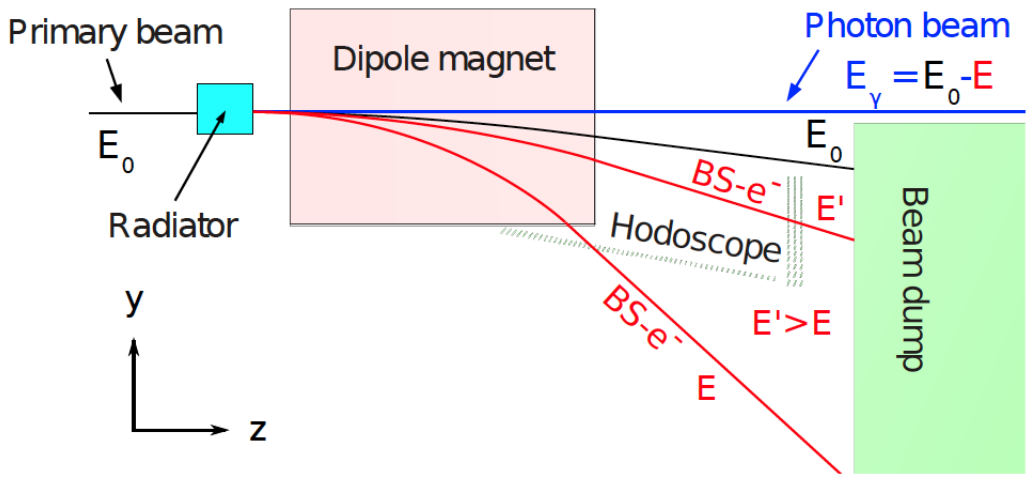

Figure 3.3: The photon tagger along with its working principle [23].

3.2.2 Central detector

After leaving the tagging system, the bremsstrahlung photon beam impinges on the target which is surrounded by the central detector. Both liquid deuterium as well as liquid hydrogen are possible as a target. However, for my work only the latter is relevant. The target is surrounded by two MWPCs[2] for track reconstruction, a scintillator barrel to veto charged particles and the BGO ball, an electric calorimeter, see Fig. 3.4. Polar angles between $\theta = 25^\circ$ and $\theta = 155^\circ$ are covered [23].

BGO ball

Forming the main part of the central detector, the BGO Rugby Ball calorimeter consists of 480 BGO[3] crystals which are organized in 15 sectors, each containing 32 crystals. Neutral and charged particles are stopped in this electromagnetic calorimeter, position and energy deposition can then be measured. Photons are detected with a remarkable energy resolution of approximately 3 %. The time resolution of the detector reaches 2 ns [23].

Scintillator barrel

The scintillator barrel is built up of 32 plastic scintillator bars which are arranged in a cylinder and attached to a photomultiplier tube. This component of the detector is designed to differentiate between charged and neutral particles. While the detection efficiency for charged particles is about 98 %, the efficiencies to detect photons or neutrons are below 1 % over a broad energy range [23]. The energy loss of the charged particles is also measured.

[2] Multi-wire-proportional-chambers
[3] Bismuth Germanate, $Bi_4(GeO_4)_3$

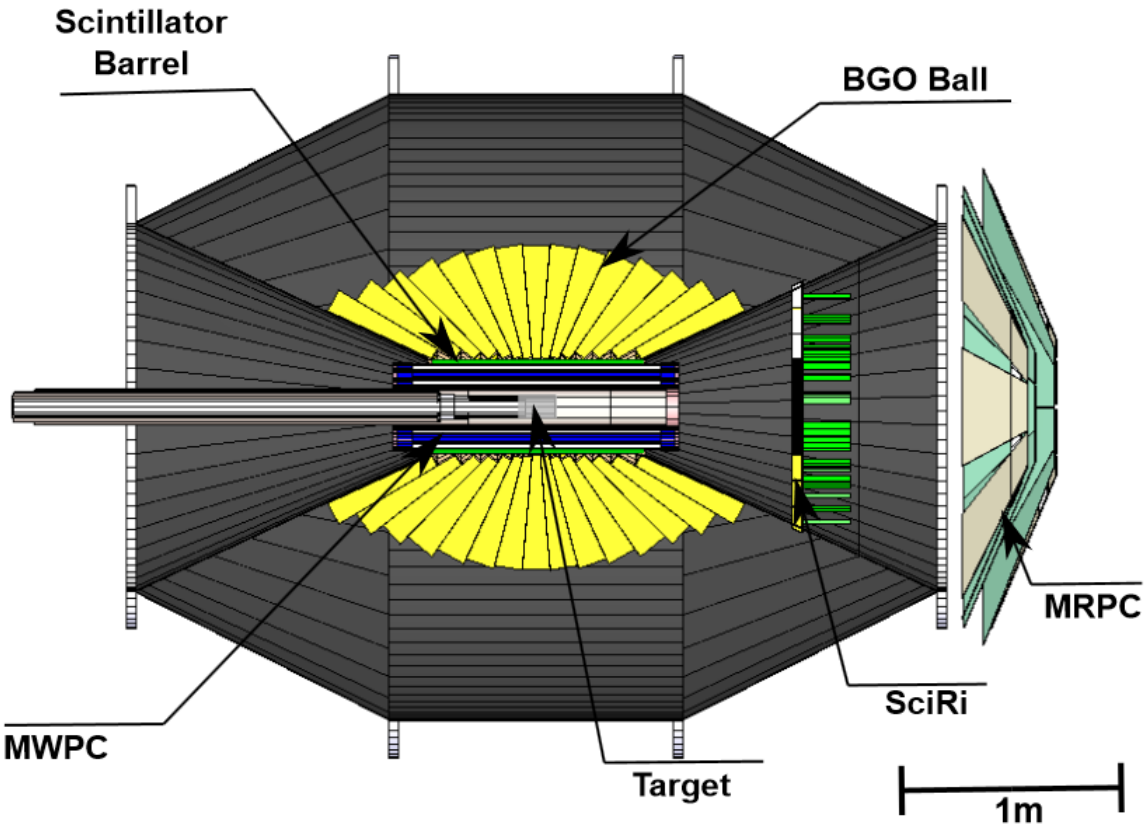

Figure 3.4: The central detector featuring the BGO Rugby ball calorimeter as its primary component among other modules [27].

MWPCs

Two MWPCs of a three-layered cylindrical shape cover the target to determine the tracks of charged particles. They are composed of inner and outer walls containing helically wound cathode strips, with anode wires positioned between them. The MWPCs were not used for this thesis, as the complex software is yet not finished [23].

3.2.3 Intermediate detectors

There are two intermediate detectors, the scintillating ring detector (SciRi) and the multi-gap resistive plate chambers (MRPC). They are used to cover the polar angular range of 10° to 25°, which is not within the acceptance of the BGO ball.

The multi-gap resistive plate chambers (MRPC) are under commissioning and are thus not used for this work. During this period, SciRi is operational and provides information about the position of charged particles. It consists of plastic scintillators arranged in rings. Avalanche photodiodes, kindly supplied by the Crystal Barrel experiment, are used for the readout [23, 28].

3.2.4 Forward spectrometer

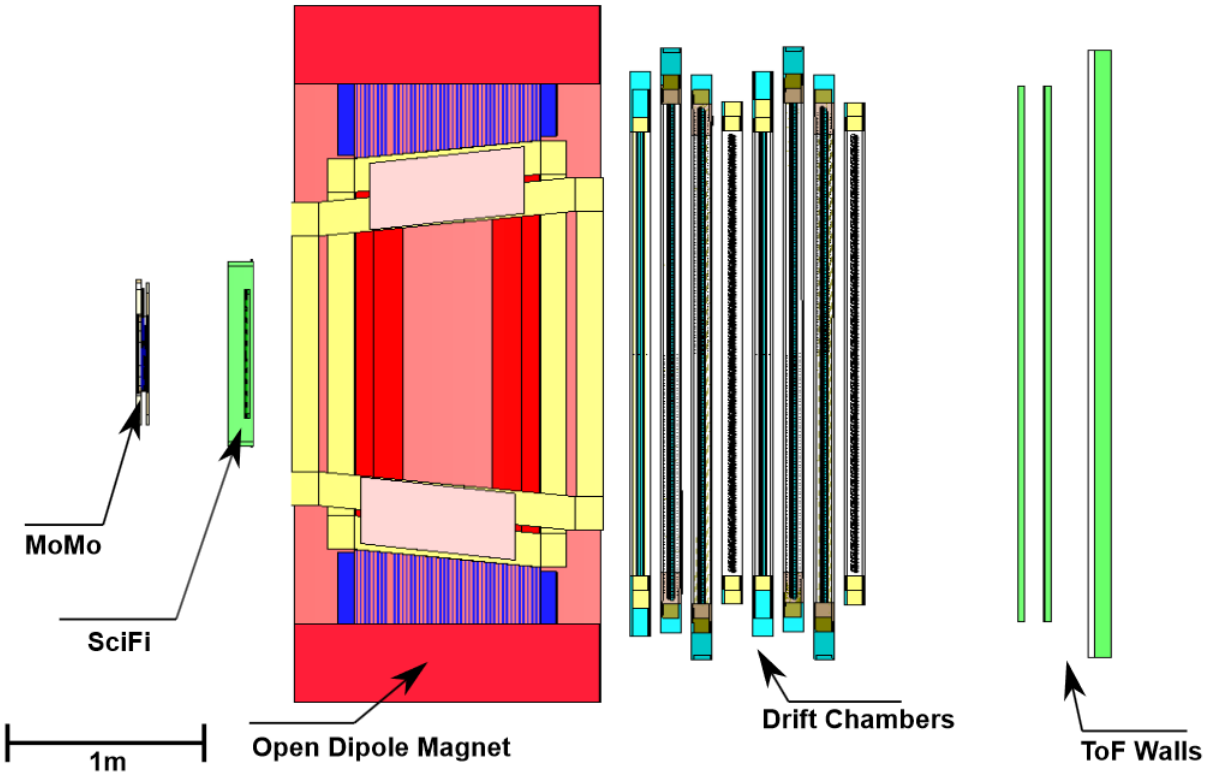

Figure 3.5: Overview of the forward spectrometer [27].

Forward-going mesons are crucial to my thesis. As the name suggests, they are detected in the forward spectrometer, the second significant component of the BGOOD detector. The smallest achievable angle is approximately 1.5° in the very forward direction, the largest angle is 11° [23, 27].

The forward spectrometer, shown in Fig. 3.5, consists of two sets of tracking detectors. The first (MoMo and SciFi) is situated in front of an open dipole magnet and the second (drift chambers) is located behind the magnet. On the right side of the figure, the Time-of-Flight (ToF) walls can be seen. Position reconstruction is performed by the detector elements both before and after the magnet. The particle trajectory is bent due to the magnetic field in the open dipole magnet. From the track radius, the momentum of the charged particles can be determined. When combined with β information obtained from the Time-of-Flight walls, this allows for particle identification.

The left histogram of Fig. 3.6 shows the reconstructed particle β against the reconstructed momentum for positively charged particles. From top to bottom, the particles π^+, K^+ and the proton are assigned to the visible curves. The right histogram depicts the calculated mass for positively charged particles.

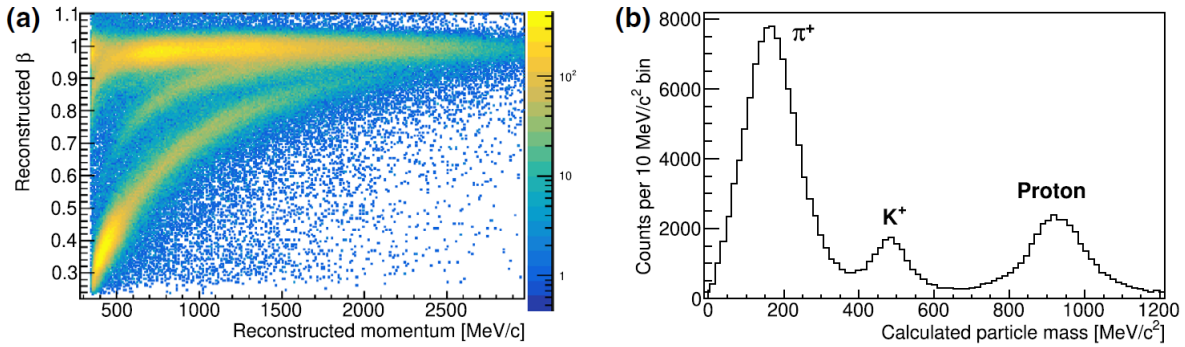

Figure 3.6: **(a)** Identification of the positively charged particles π^+, K^+ and p from top to bottom in the forward spectrometer [23]. **(b)** The same particles classified by their masses calculated using momentum and β [23].

MOMO and SciFi

MOMO and SciFi are both placed in front of the OD magnet and are scintillating fiber detectors, with MOMO having 672 fibers and SciFi using 640 fibers that are connected to photomultipliers. These are organized into three or two layers to get information about the particle position. Central openings of a radius of 4.5 cm and dimensions of 4 cm × 4 cm, respectively, allow the beam to pass without interaction [23].

Drift chambers

The tracking of the charged particles is continued behind the open dipole magnet. Eight drift chambers with four different orientations indicated by u, v, x and y are used. To allow the beam to pass through, the wires are made inactive in the central region [23].

Time-of-Flight walls

The forward spectrometer is concluded by a Time-of-Flight measurement. This part of the detector is composed of three walls of plastic scintillators divided into horizontal bars. These walls have gaps, so that the beam can pass through and to prevent signals arising from the abundant production of e^+e^- pairs. Photomultipliers are again used for the readout. The β of the particles can be measured, and this information, along with the momentum, is necessary for particle identification [23].

3.2.5 Photon flux monitor

In Fig. 3.2 one can see that the last part of the BGOOD setup is the flux monitoring. Two detectors, the Flux Monitor, abbreviated by FluMo and the Gamma Intensity Monitor, in short GIM, are used to measure the relative and absolute flux rate, respectively. This quantity is indispensable for the determination of cross sections.

GIM operates at low rates to prevent radiation damage. The detector material employed is lead glass with complete absorbance capability. FluMo consists of five scintillators that detect a certain fraction of the flux. This fraction can be determined in dedicated calibration runs together with GIM and low rates. The flux for high rates can then be calculated using the measurements that are continuously done by FluMo. Both detectors, GIM and FluMo, observe e^+e^- pairs from pair production happening upstream in the experiment [23].

CHAPTER 4

Reconstruction of $\gamma p \rightarrow K^{+}\Lambda(1405)$

In this thesis, I study the reaction: $\gamma p \rightarrow K^{+}\Lambda(1405)$. Fig. 4.1 shows a possible Feynman like diagram for this reaction. Time goes from left to right. The incoming photon impinges on a proton target, so that an intermediate hyperon state, Y^{*}, is created via the off-shell kaon. It decays directly into $(\Sigma\pi)^{0}$. The branching ratio for the three possible finals states, $\Sigma^{+}\pi^{-}$, $\Sigma^{0}\pi^{0}$ and $\Sigma^{-}\pi^{+}$, is $33.\overline{3}$ % each. The decay scheme for the case where $\Lambda(1405) \rightarrow \Sigma^{+}\pi^{-}$, which is investigated in this thesis, is illustrated in Fig. 4.2. The decay of Σ^{+} results in the production of a proton and a neutral pion. This pion, in turn, can be detected through the emission of two photons.

The main task was to identify the various final state particles, which are: K^{+}, π^{-}, π^{0}, p, in the different parts of the detector. This involved data analysis techniques applied to Monte-Carlo-simulated datasets and to real datasets obtained from the beam time in June 2018.

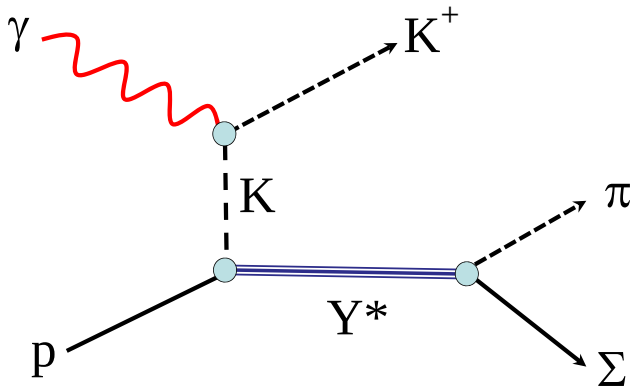

Figure 4.1: Photoproduction of the $\Lambda(1405)$ resonance in a t-channel exchange. Time goes from left to right [16].

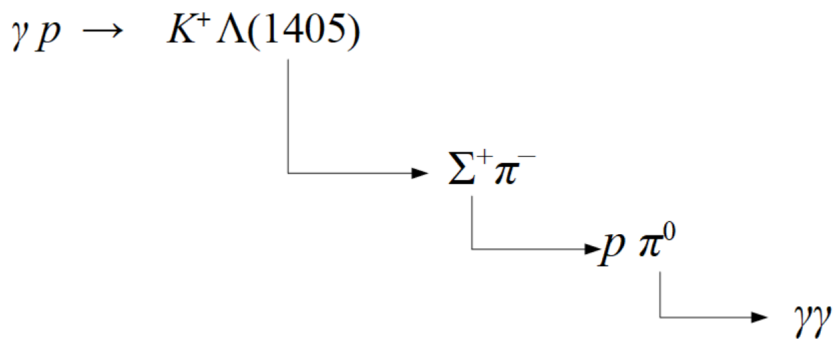

Figure 4.2: Decay scheme for the $K^+\Lambda(1405)$ photoproduction focusing on one specific charged channel: $\Lambda(1405) \rightarrow \Sigma^+\pi^-$.

4.1 Software

The analysis framework that is used at the BGOOD experiment is ExPlORA[1] [29]. This comprehensive framework is capable of handling both real data and simulated data. It is plugin-based, allowing for modular and flexible analysis adapted for specific research needs. The primary programming language used in ExPlORA is C++. It extends the object-oriented ROOT framework [30], developed by CERN, which is used worldwide for data analysis and to perform simulations in high-energy physics research. Its data is structured in so-called trees that enable to access fast to large datasets. The histograms shown in this thesis are also made within the ROOT framework using graphical tools. In Section 5, the utilization of RooFit [31], a toolkit for statistical modeling and fitting provided within the ROOT framework, will be explained in more detail.

4.2 Particle identification

In the following sections, the identification of the charged and neutral final state particles is described. The K^+ is identified in the forward spectrometer, the π^0 from two photons in the BGO, and the p and π^- can either be reconstructed in the BGO or in SciRi.

4.2.1 Identification of the K^+

The identification of kaons is performed within the forward spectrometer. This enables the analysis of events occurring at very forward angles. The mass is selected by plotting the invariant mass in the forward spectrometer and by looking at the 2σ range around the kaon mass, see Fig. 4.3. Particles observed in the forward spectrometer with a mass between 450 MeV and 550 MeV are considered as kaon candidates. Finally, a cut on the cosine of the polar angle θ with respect to the kaons was made to consider events only in the range $0.9 < \cos\theta^{K^+}_{\mathrm{CM}} < 1.0$, so extremely forward going particles.

[1] **Ex**tended **Pl**uggable **O**bject-oriented **R**OOT-ified **A**nalysis

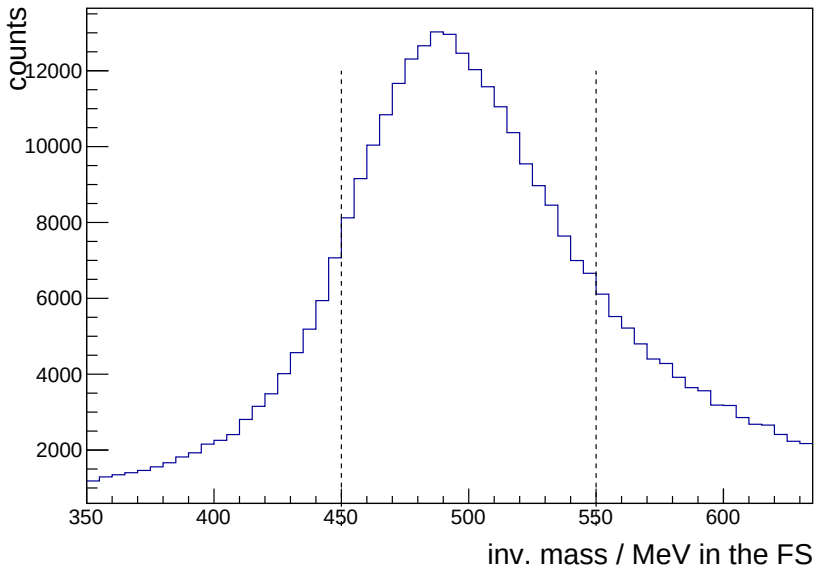

Figure 4.3: Invariant mass distribution in the forward spectrometer used to determine the value for the kaon mass selection. The vertical dashed lines indicate the 2σ range around the kaon mass.

4.2.2 Identification of the π^0

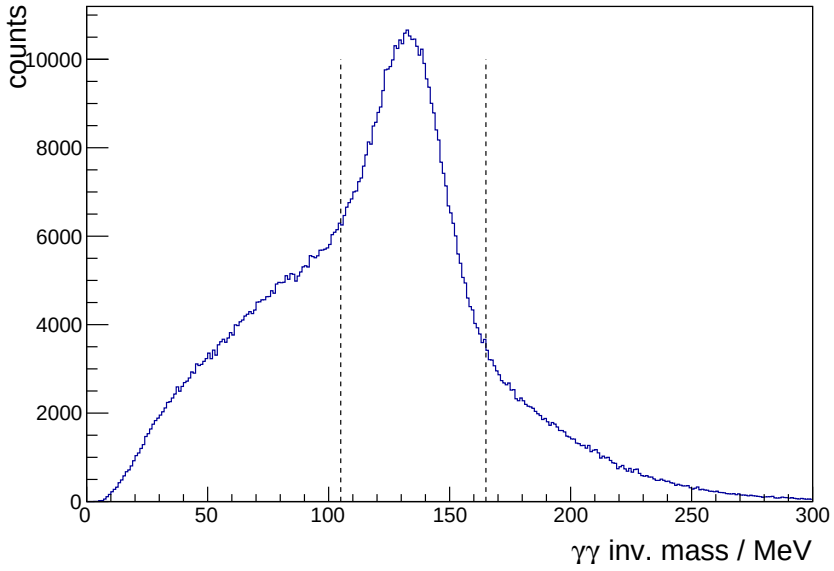

Figure 4.4: Invariant mass distribution of photon pairs used to determine the value for the pion mass selection. The vertical dashed lines indicate the 2σ range around the pion mass.

Neutral pions are identified by requiring exactly two photons in the BGO calorimeter. In order to estimate an adequate value for a mass selection, the invariant mass distribution of photon pairs was plotted. For this purpose, the invariant mass of the photon pairs is determined using the sum of the four-momenta of the two photons. Fig. 4.4 shows the invariant mass of the photon pairs for simulated data. Events are selected with a $\gamma\gamma$ invariant mass between 105 MeV and 165 MeV, which represents the 2σ range around the pion mass and that is indicated by the vertical dashed lines.

4.2.3 Identification of the p and of the π^-

The reconstruction of the remaining charged particles, i.e., the proton and the negative pion is much more difficult. These particles can be detected either in the BGO or SciRi. However, it is not possible to directly discern which one corresponds to the proton and which one is the pion, since only direction information can reliably be used.

To determine the four-momentum, a system of two simultaneous equations, 4.1 and 4.2, is required involving the unit vectors of these particles, $\hat{p}_1$ and $\hat{p}_2$, which are multiplied by their magnitudes k_1 and k_2:

$$0 = p_{\mathrm{k}}^x + p_{\pi^0}^x + k_1\hat{p}_1^x + k_2\hat{p}_2^x \tag{4.1}$$

$$p_\gamma^z = p_{\mathrm{k}}^z + p_{\pi^0}^z + k_1\hat{p}_1^z + k_2\hat{p}_2^z \tag{4.2}$$

The equations can be derived from momentum conservation. The incoming momentum p_{in} is equal to the z-component of the beam momentum p_γ^z, as the target is at rest and the beam goes in z-direction. One needs to solve the simultaneous equations for k_1 and k_2. The quantities p_{k}, p_{π^0}, $\hat{p}_1$ and $\hat{p}_2$ are measured. Knowing the magnitude one can calculate the three-momenta. Using the masses of the proton and the negative pion one can determine the four-momenta.

At this stage, a first assignment of the proton and pion to particles 1 and 2 must be established. Since it is not known, which particle is which, two combinations are possible: particle 1 = proton, particle 2 = pion or particle 1 = pion, particle 2 = proton. In order to decide, which combination is the correct one, the angles between the different particle tracks were considered. Fig. 4.5 is a simple sketch to get a better idea of the track angles. Only the particles $\Lambda(1405)$, Σ^+, p and π^- are shown here. Their prolonged tracks are illustrated with dashed lines. The $\Lambda(1405)$, shown in green, decays into a π^-, illustrated in orange. It also decays into a Σ^+, marked in violet, which then decays into a proton, indicated in blue, and the not shown π^0. Due to their almost equal masses, these three particles propagate in a similar direction, as indicated in the sketch. The proton track is shown as a blue, solid arrow. The angle between the proton track and the $\Lambda(1405)$ track, ϵ_1, must be smaller than the angle between the π^- and the $\Lambda(1405)$ track, ϵ_2, since the π^- goes in a different direction than the proton or the $\Lambda(1405)$. This is explained by the fact that the π^- has a significantly smaller mass than the $\Lambda(1405)$ or the proton. ϵ_1 and ϵ_2 are calculated for both particle combinations, the case where $\epsilon_1 < \epsilon_2$ is assumed to be the correct assignment, while the case where $\epsilon_1 > \epsilon_2$ is assumed as the wrong assignment.

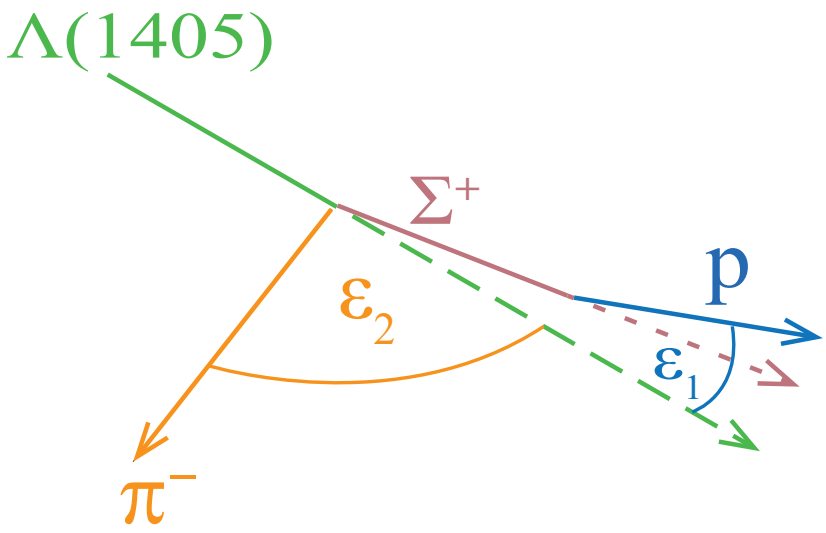

Figure 4.5: Sketch of the particle tracks and track angles. For simplicity, not all of the particles contributing to the reaction are shown. The $\Lambda(1405)$ track is marked in green. It decays into a π^-, shown in orange and a Σ^+, shown in violet. The proton, marked in blue, is one of the final particles from the Σ^+. The angle between the proton and the $\Lambda(1405)$ track is ϵ_1. The angle between the π^- and the $\Lambda(1405)$ track is ϵ_2.

One can verify if this method of assigning the proton and the pion works by plotting the invariant mass of the $p\pi^0\pi^-$ system. If the particles are assigned correctly, there must be a maximum of the distribution at the mass of the $\Lambda(1405)$. The absence of this maximum means that the assignment is not correct. Fig. 4.6 and Fig. 4.7 show the $\pi^-\pi^0 p$ invariant mass distributions for the correct and the wrong assignment, respectively, for Monte-Carlo-simulated $\gamma p \rightarrow K^+\Lambda(1405)$. The correct assignment leads to a distribution where a prominent peak is seen at the expected $\pi^-\pi^0 p$ invariant mass. On the contrary, the result for the wrong assignment does not exhibit a significant peak at the expected value for the invariant mass. Thus, it can be concluded that this method works rather well.

Nevertheless, this method provides only a limited, good possibility to identify the proton and the negative pion. By looking for example at Fig. 4.7, one sees that the distribution at the $\Lambda(1405)$ mass is not zero. An assignment that works 100 % correctly is thus not possible here.

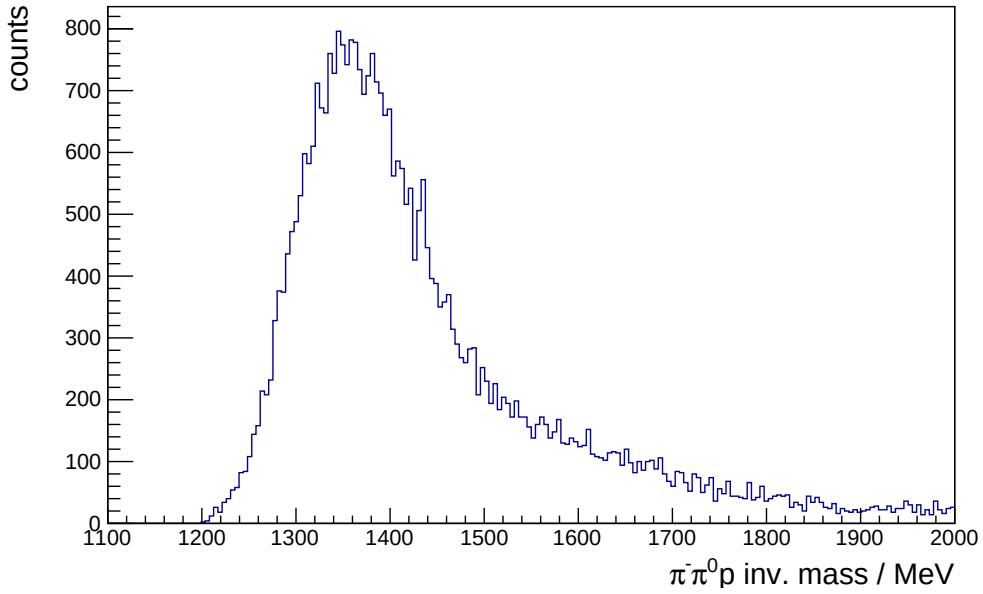

Figure 4.6: $\pi^-\pi^0 p$ invariant mass distribution for the case of a "correct π^-/p assignment".

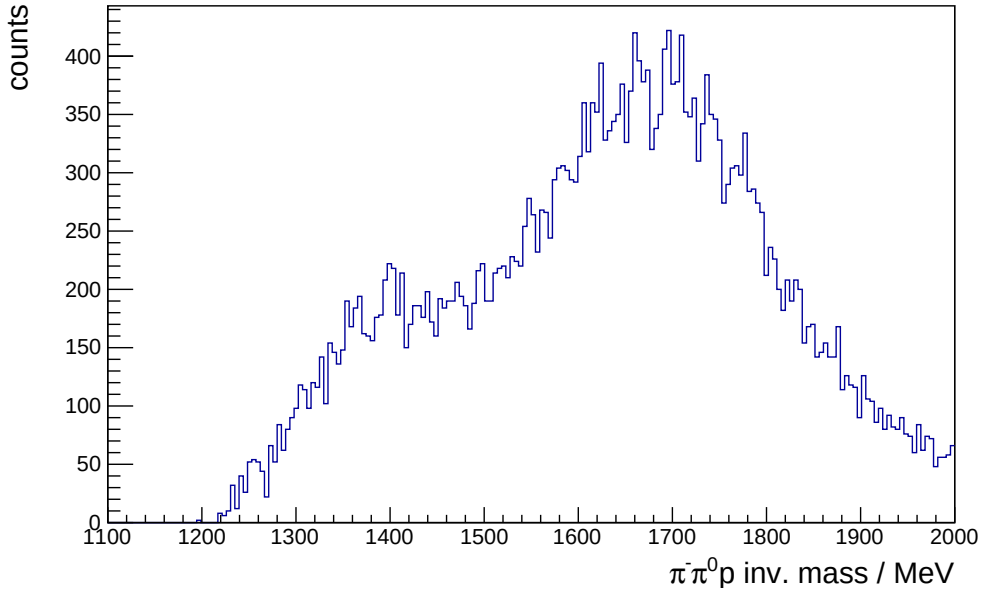

Figure 4.7: $\pi^-\pi^0 p$ invariant mass distribution for the case of a "wrong π^-/p assignment".

4.2.4 Σ^+ selection

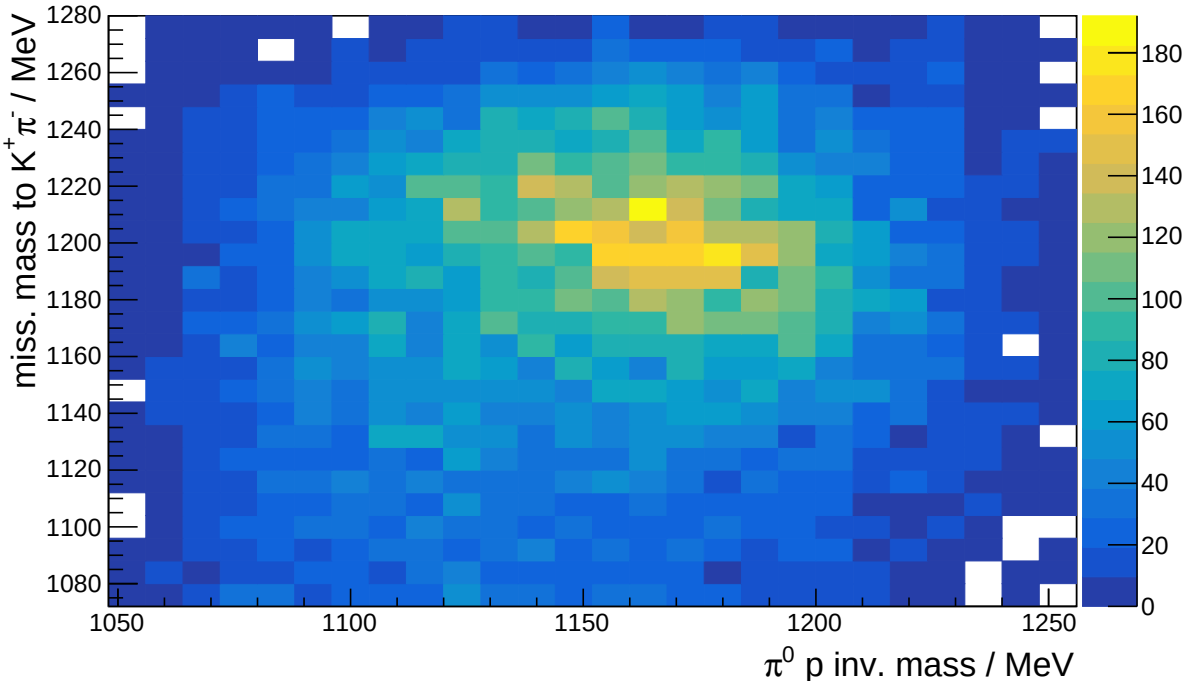

Figure 4.8: Missing mass to $K^+\pi^-$ versus πp invariant mass.

In order to get a clean signal, the Σ^+ can also be identified. The missing mass to the $K^+\pi^-$ is plotted against the $\pi^0 p$ invariant mass using Monte-Carlo-simulated data for $\gamma p \to K^+\Lambda(1405)$. The histogram is shown in Fig. 4.8. On both axes, a peak at the Σ^+ mass is expected and observed. Only events with a $\pi^0 p$ invariant mass between 1 110 MeV and 1 210 MeV and a missing mass to $K^+\pi^-$ between 1 150 MeV and 1 250 MeV are considered for the future steps.

CHAPTER 5

Extraction of the yield

Once all these cuts are applied, the photon beam energy can be plotted in dependence of the missing mass to the K^+. This histogram will be needed for the extraction of the yield. The 2D histogram for the real data is shown in Fig. 5.1. A projection on the missing mass to K^+ for the y bin range 57 – 59 and for an energy range from 1 755 MeV to 1 810 MeV is depicted in Fig. 5.2. A signal is clearly visible around 1 405 MeV but contains a contribution from the $\Sigma(1385)$ resonance. As both masses are very similar and both baryons can decay into the same channel, they are hardly distinguishable. Right to the prominent peak, the $\Lambda(1520)$ resonance is visible.

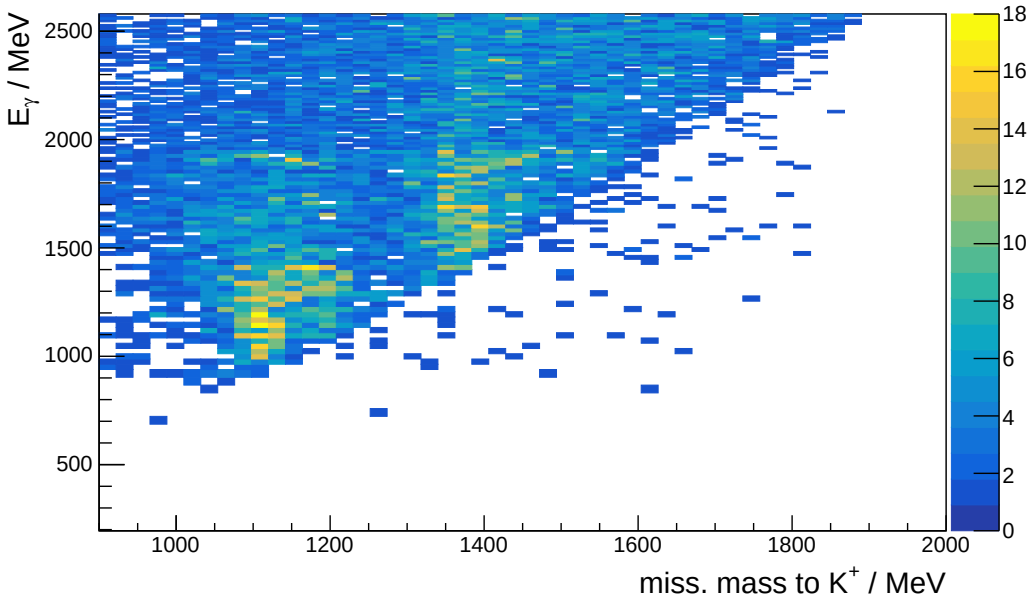

Figure 5.1: Photon beam energy versus the missing mass to the K^+ for real data from June 2018.

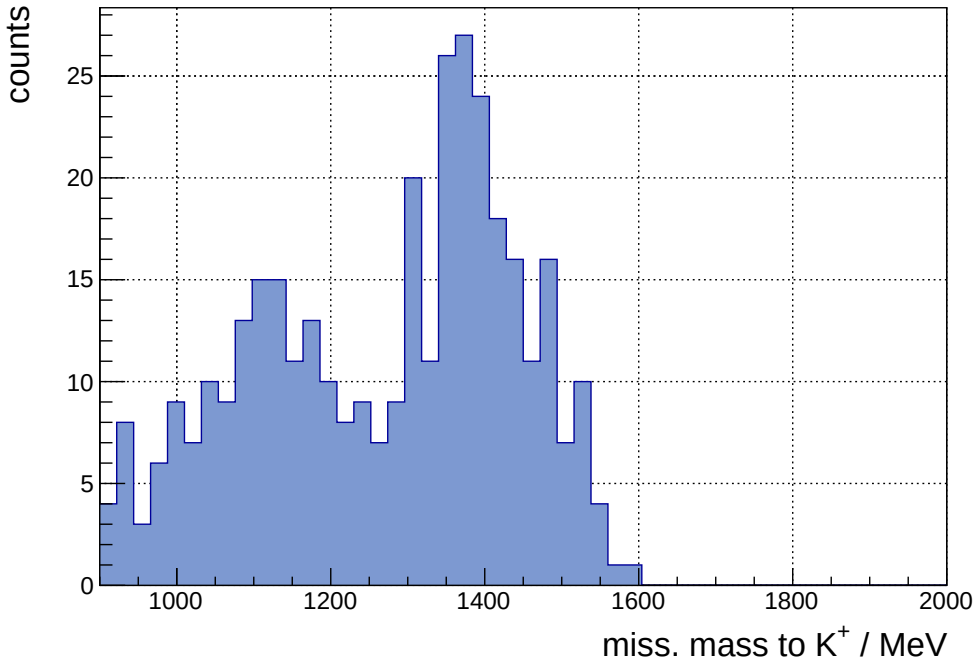

Figure 5.2: Missing mass to K^+, for the y bin range 57 − 59 and for a beam energy range of 1 755 MeV − 1 810 MeV, with angles $\cos\theta^{K^+}_{\mathrm{CM}} > 0.9$.

Left to the signal, the background distribution is seen. Most of the background comes from misidentified π^+. The identification of positively charged particles was shown in Fig. 3.6, in Chapter 3.2.4. The yellow bands for the pion and the kaon are very close to each other, even a little overlapping making it hard to always distinguish between them correctly. In order to simulate the background, negative charge tracks in the forward spectrometer are taken. Since there are no negative kaons, these negative charge tracks must be π^-. This gives a good description for the background, since the π^- spectra are equal to the π^+ spectra.

Another important source for the background is the reaction $\gamma p \rightarrow K^+\Sigma(1385)$, where the $\Sigma(1385)$ decays into $\Sigma^+\pi^-$. As already mentioned, this resonance is very hard to distinguish from the $\Lambda(1405)$ resonance as their masses are close to each other and their final state particles are the same.

The background needs to be reduced. The procedure is to differentiate between background and signal, and then to subtract the background from the signal. Different methods for this are presented in the Sections 5.1 and 5.2.

In the following, two methods for extracting the yield are presented. The first method is the yield extraction by means of the RooFit toolkit which was described in 4.1. RooFit uses template fits to scale provided signal and background spectra to fit the data. The second method uses sideband subtraction. The background that comes from misidentified π^+ is scaled to the background included in the real data and then subtracted. In this approach, and in contrary to the RooFit method, no other simulations, e.g. $\Lambda(1405)$, are used. The real data and the background from misidentified π^+ presented in this method are the same as for the yield extraction with RooFit.

In the end, the yield and corresponding error of the remaining signal is calculated as a function of photon beam energy from 1339 to 1 638 MeV, which is the range where signals from the $\Lambda(1405)$ resonance are observed.

5.1 RooFit method

For this method, the usage of the RooFit toolkit is essential. Included in the fit is background from misidentified π^+, simulated $\Lambda(1520)$, $K^+\Sigma^0$ and $\Lambda(1405)$ together with simulated $\Sigma(1385)$. This means, that the simulation for $\gamma p \to K^+\Lambda(1405)$ was chosen but has a contribution from $\gamma p \to K^+\Sigma(1385)$. The respective contribution of both particles is again not distinguishable here.

The fit is performed between 1 339 MeV and 1 638 MeV. Each energy bin corresponds to three tagger bins. An example is shown in Fig. 5.3 for a photon beam of 1 583 MeV. The other fits can be found in Appendix A.

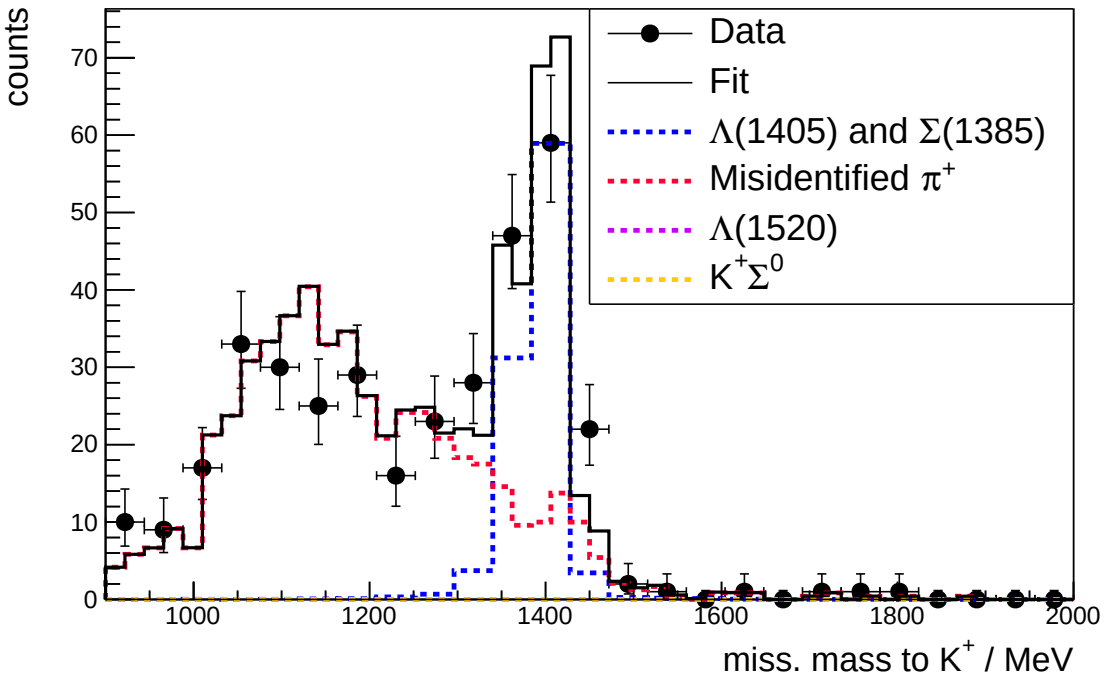

Figure 5.3: RooFit for $E_\gamma = 1\,583$ MeV. Data points are shown as black circles, the full fit as a black solid line. Background channels are depicted as colored dashed lines. The main contribution comes from π^+ misidentified as K^+ (red dashed line).

As one can see, the background on the left of the $\Lambda(1405)$ peak can already be well described by π^+ that are misidentified as K^+. For some beam energies, it is better described, when the simulation for the $K^+\Sigma^0$ is included. Next to the signal peak, a smaller peak coming from the $\Lambda(1520)$ can be seen for energies close to its threshold.

5.2 Sideband method

Another way to extract the yield is the sideband subtraction. Only the background that comes from misidentified π^+ is taken into consideration. Figure 5.4 is an example for a beam energy of 1 583 MeV that depicts this background and the data.

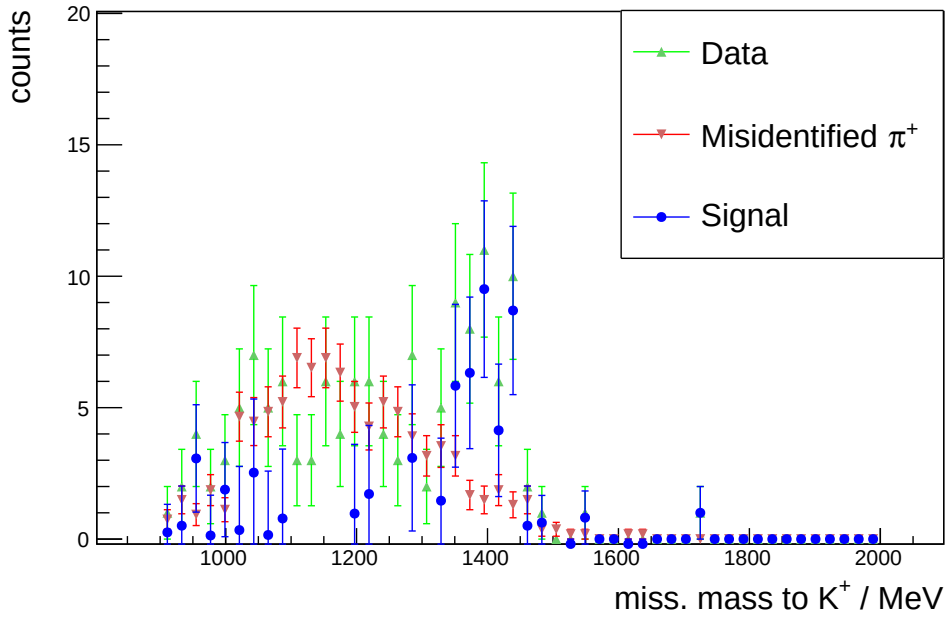

Figure 5.4: Data, background and signal distribution for $E_\gamma = 1\,583\,\text{MeV}$. The background from the misidentified π^+ was scaled such, that it describes the green data. Afterwards, it is subtracted from the data, the remaining signal is shown in blue.

Initially, the background from the misidentified π^+, that is shown in red, is higher than the background observed in the real data, which is illustrated in green. This is due to the fact, that the misidentified π^+ are simulated via the misidentified π^-. Their spectra are equal in shape but the counts differ. In order to describe the green background, the red spectrum is scaled such, that the integrals of both, red and green spectra, agree in the range from $900 - 1\,200\,\text{MeV}$. This is done by multiplying the red spectrum with the integral of the green spectrum and then dividing by the integral of the red spectrum. The red spectrum is then subtracted from the real data leaving only the signal, demonstrated in blue. The integral of this blue distribution is determined for photon beam energies between 1339 and $1\,638\,\text{MeV}$ enabling the extraction of the yield for the determination of the differential cross section.

5.3 Yield

The extracted yield is shown for both methods in Fig. 5.5. The result obtained using RooFit is illustrated in red and the yield extracted with the Sideband method is depicted in blue. The values of the first three data points are very similar for both methods. However, for higher photon beam energies, the values differ more. This could be explained by the fact that the RooFit method takes more background channels into account, for example, the simulated $\Lambda(1520)$, whereas the Sideband method only uses information from the background coming from misidentified π^+.

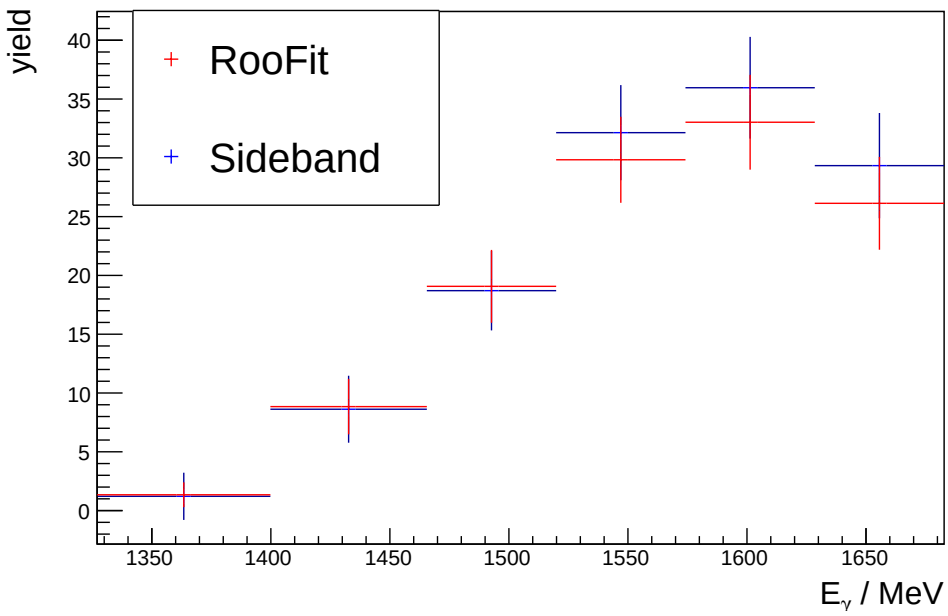

Figure 5.5: Yield for RooFit method in red and Sideband method in blue.

CHAPTER 6

Determination of the differential cross section

The central aspect of this thesis is to determine the differential production cross section for $\gamma p \rightarrow K^+\Lambda(1405)$. Equation 6.1 is the formula for the determination of the cross section. It contains the yield $N_{\mathrm{K}}(E_\gamma, \theta)$, the photon flux $N_\gamma(E_\gamma, \theta)$, the detection efficiency ϵ, the target area density ρ, as well as the solid angle Ω. The yield was already determined in Chapter 5. The remaining quantities will be introduced in the following.

$$\frac{d\sigma}{d\Omega} = \frac{N_{\mathrm{K}}(E_\gamma, \theta)}{N_\gamma(E_\gamma, \theta) \quad \epsilon \quad \rho \quad \Omega} \tag{6.1}$$

6.1 Target area density and solid angle

The target area density can be calculated using the proton density of $4.237 \times 10^{-8}\,(1/(\mu\mathrm{b} \cdot \mathrm{cm}))$ multiplied by the effective target length, 11.1 cm for the data set from June 2018 [15]. This leads to the following value for the target area density, used for this thesis:

$$\rho = 4.7 \times 10^{-7}\,\frac{1}{\mu\mathrm{b}}$$

To obtain the solid angle, an integration over the polar angle, θ_{CM}, and the azimuthal angle, ϕ, needs to be carried out [15]:

$$\begin{aligned}\Omega &= \int_{\phi_{\mathrm{a}}}^{\phi_{\mathrm{b}}} \int_{\theta_{\mathrm{CM,A}}}^{\theta_{\mathrm{CM,B}}} \sin(\theta_{\mathrm{CM}}) \mathrm{d}\theta_{\mathrm{CM}} \mathrm{d}\phi \\ &= 0.2\pi\end{aligned}$$

Here, a, A and b, B are used to define the limits of the integrals. As the focus is put on forward angles, the range $0.9 < \cos(\theta_{\mathrm{CM}}) < 1.0$ is considered.

6.2 Detection efficiency

The detection efficiency is another important parameter in the cross section determination. It is the probability that a reaction which took place is observed and reconstructed. It depends on the detector efficiency, the analysis and the branching ratios. The detection efficiency is determined using Monte-Carlo-simulated $\gamma p \rightarrow K^+\Lambda(1405)$. The number of the events that are finally detected (reconstructed events) is divided by the total number of generated events (input events).

The input events are given by the total number of generated events with $\cos\theta^{K^+}_{\mathrm{CM}} > 0.9$, in dependence of the beam energy. In order to obtain the reconstructed events, a 2D histogram of the beam energy in dependence of the missing mass to the positive kaon is created. With this, 1D histograms for different energies can be created. This was already discussed in section 5 in more detail.

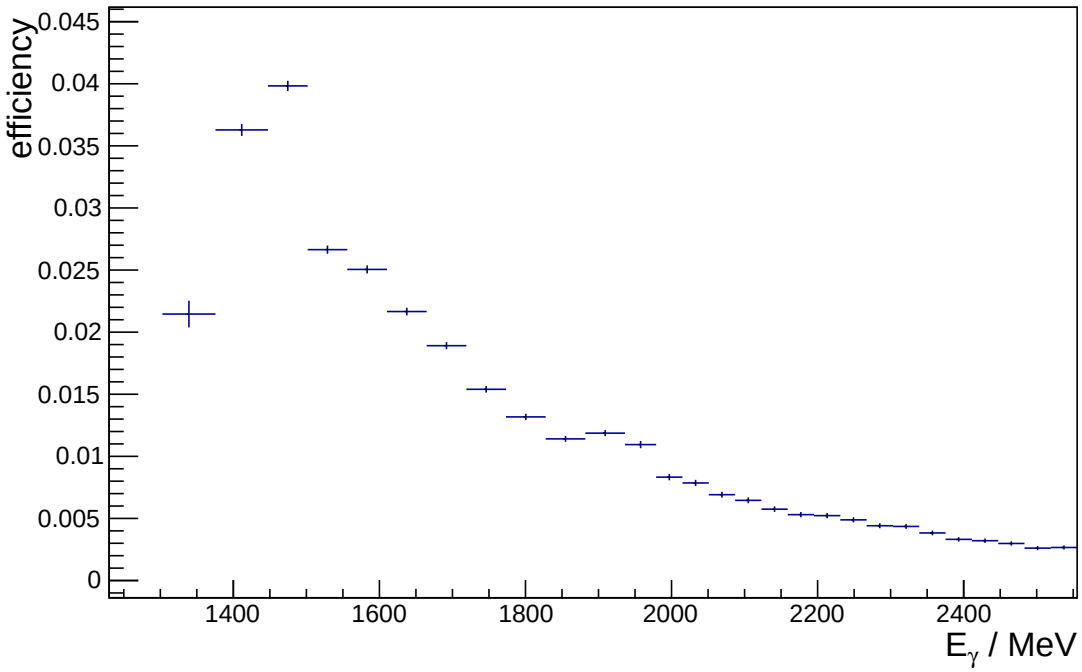

Figure 6.1: Detection efficiency in dependence of the photon beam energy. Three bins are grouped together.

Fig. 6.1 depicts the determined detection efficiency. As expected, it has a peak at lower beam energies, at about 1 500 MeV. This is due to the fact, that the detection efficiency was determined using Monte-Carlo-simulated data for $\gamma p \rightarrow K^+\Lambda(1405)$. With increasing beam energy the efficiency seems to decrease exponentially.

6.3 Differential cross section for $\gamma p \rightarrow K^+\Sigma^+\pi^-$

First, the differential cross section for $\gamma p \rightarrow K^+\Sigma^+\pi^-$ was determined via the Equation 6.1, divided by 3, since there are three decay channels with equal branching ratios. This is thus not the cross section for the total process, $\gamma p \rightarrow K^+\Lambda(1405)$, which will be dealt in Section 6.5.1, since a contribution from the reaction $\gamma p \rightarrow K^+\Sigma(1385)$ is still included.

As discussed in Section 5, the yield was extracted via two different methods, using the RooFit toolkit and applying sideband subtraction. Fig. 6.2 shows the result for the differential cross section obtained with the RooFit method in red and with the Sideband method in blue. The x-values have been converted from beam energy to the Center-of-Mass energy W. As expected, the general trend shows an increase with rising energies.

At the first three data points, the values of both methods are very close to each other, thus the red data points are barely visible. The values of the last three points show differences between the two methods. As already explained in Section 5, this could be due to the fact that the RooFit method includes more background channels than the Sideband method.

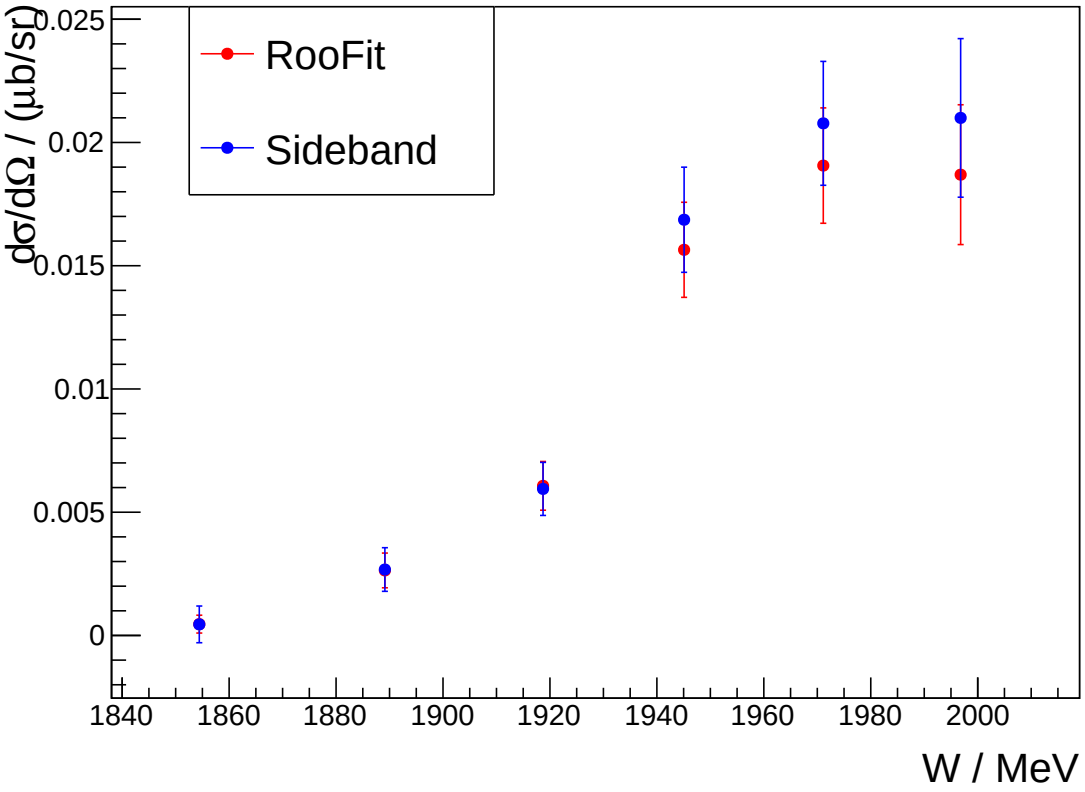

Figure 6.2: Differential cross sections for $\gamma p \rightarrow K^+\Sigma^+\pi^-$. In red, RooFit method for yield extraction, in blue, Sideband method.

6.4 Contribution of Σ(1385)

Until now, only the cross section for $\gamma p \rightarrow K^+\Sigma^+\pi^-$ was determined. $\Lambda(1405) \rightarrow \Sigma^+\pi^-$ is one of the three possible decay channels of the $\Lambda(1405)$ resonance. However, the $\Sigma(1385)$ can decay into the same particles. This means that the presented results for the differential cross section contain a non-negligible contribution from $\Sigma(1385)$ which must be removed.

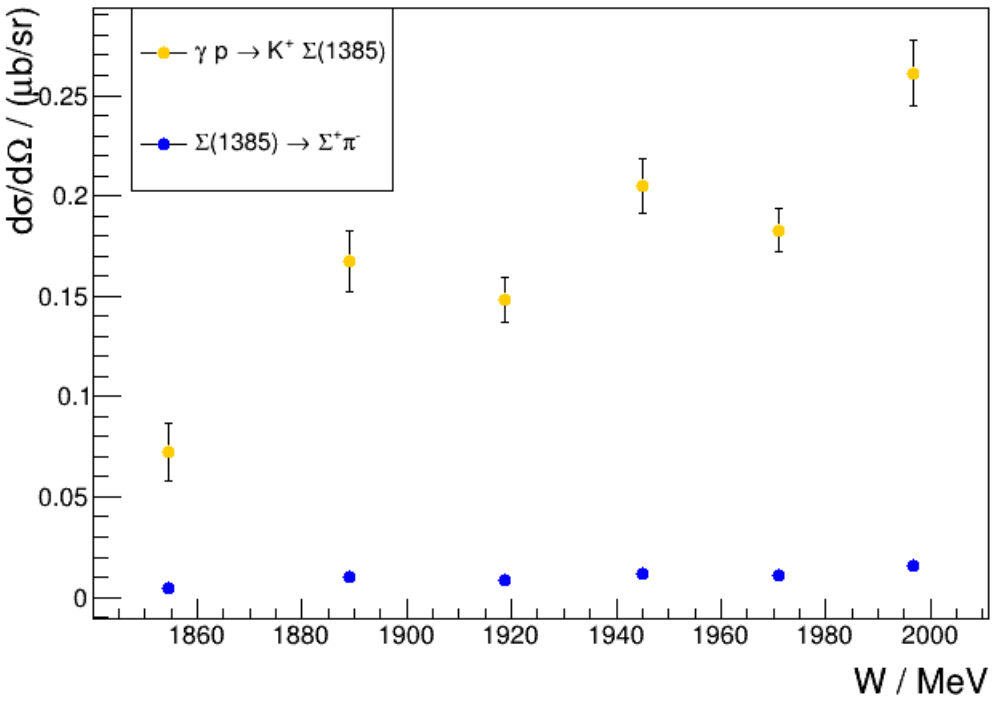

Figure 6.3: Differential cross section for $\gamma p \to K^+\Sigma(1385)$ in yellow and the scaled cross section in blue where $\Sigma(1385) \to \Sigma^+\pi^-$ is the relevant decay channel. To obtain the blue cross section result, the yellow cross section was scaled by $(0.117 \cdot 0.5)$. The error bars are too small to be seen. The figure was created using data from June 2018 provided by M. Jena during his master's thesis [32].

The differential cross section for $\gamma p \to K^+\Sigma(1385)$ has been determined at BGOOD using the same experimental setup as for the analysis of the $K^+\Lambda(1405)$ photoproduction. The angular range is also the same, i.e., $0.9 < \cos(\theta)^K_{\mathrm{CM}} < 1.0$. The result that uses data from 2017 is shown in Appendix C. In this thesis only data from 2018 was used. Besides, three bins were grouped together.

The $\Sigma(1385)$ decays into $\Lambda\pi$ with a branching ratio of $(87.0 \pm 1.5)\,\%$ and into $\Sigma\pi$ with a branching ratio of $(11.7 \pm 1.5)\,\%$ [33]. Thus, the cross section result must be scaled by 0.117. Furthermore, this decay mode needs to be specified. A decay into $\Sigma^0\pi^0$ is forbidden by isospin conservation rules. However, a decay into $\Sigma^+\pi^-$ and into $\Sigma^-\pi^+$ is possible, with a branching ratio of 50 % each. This value was determined by means of the Clebsch–Gordan coefficients [34]. Thus, the differential cross section must additionally be scaled by 0.5. With this, one obtains the fraction of the $\Sigma(1385)$ photoproduction cross section that has to be subtracted from the cross section result for $\gamma p \to K^+\Sigma^+\pi^-$. Fig. 6.3 shows the cross section for $\gamma p \to K^+\Sigma(1385)$ in yellow and this cross section scaled by $(0.117 \cdot 0.5)$ in blue. The error bars are too small here, therefore they are not visible in this figure. It can clearly be seen that the scaled cross section is rather small. Nevertheless, it has a significant contribution to the analysis of the $K^+\Lambda(1405)$ photoproduction, and thus needs to be considered.

In order to get an impression of how much the cross section for $\gamma p \to K^+\Sigma^+\pi^-$ is reduced due to the subtraction of the contribution from $\Sigma(1385)$, Fig. 6.4 was created. It shows the cross section before the subtraction of the contribution from $\Sigma(1385)$ and the corresponding result after the subtraction, for the RooFit method. Please note, that the latter is not the result for the photoproduction cross section, since it still needs to be scaled by 3, see Section 6.5.1. The results for the Sideband method are demonstrated

in Fig. 6.5. It is clearly visible that the contribution of Σ(1385) causes a slight shift of the data points. Furthermore, it can be stated that the first three values are below zero due to the subtraction.

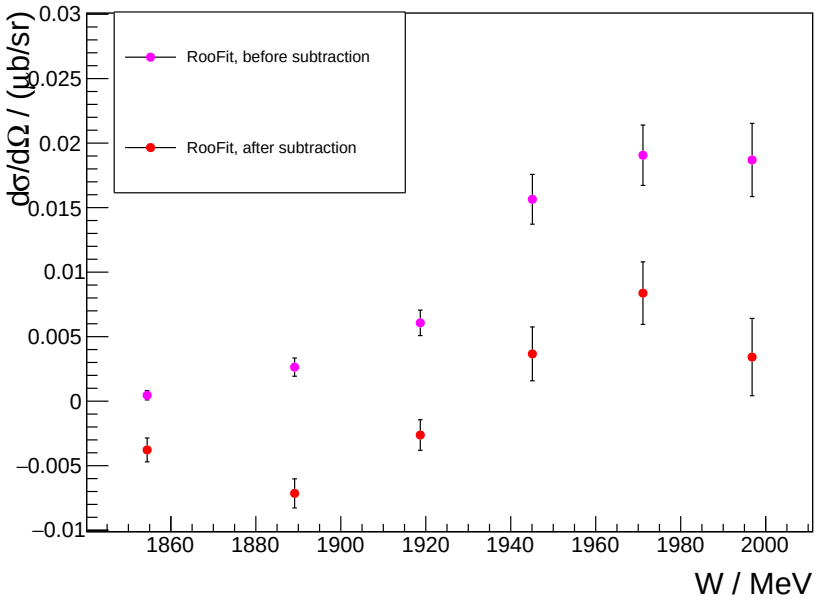

Figure 6.4: In pink: differential cross section for $\gamma p \rightarrow K^+\Sigma^+\pi^-$, determined with the RooFit method. This is the result before the subtraction of the Σ(1385) contribution. In red is shown the result after the subtraction.

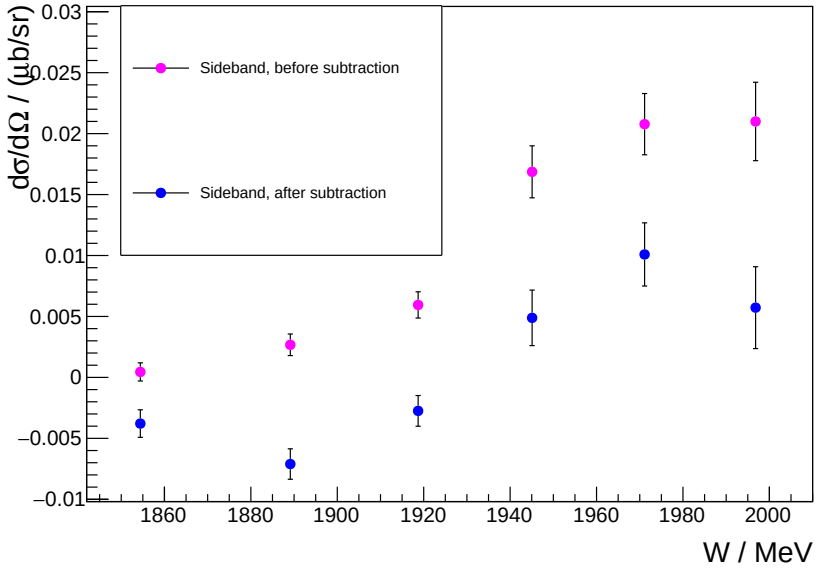

Figure 6.5: In pink: differential cross section for $\gamma p \rightarrow K^+\Sigma^+\pi^-$, determined with the Sideband method. This is the result before the subtraction of the Σ(1385) contribution. In blue is shown the result after the subtraction.

6.5 Systematic uncertainty estimation

Before discussing the final cross section results in Section 6.5.1, the systematic uncertainty will be estimated. This estimation includes several steps. At first, the two methods that were used to determine the yield, the RooFit and the Sideband method, should be compared. In order to see how much both results deviate from each other, the ratio of the cross sections determined in Section 6.3 can be plotted and a constant linear curve can be fitted to the data points. This is seen in Fig. 6.6. The first error bar is particularly large, which can be explained by the fact that the data points from both cross sections are very close to zero. In the error propagation this leads to big values. The constant curve, that was fitted to the data, is shown in green. If it is close to 1, the two methods for the yield extraction are similar. The result of the fit is $f(x) = 0.93$ with a fit error of ± 0.09. This means a deviation from 1 of 7 %. This is the first part of the uncertainty estimation. Furthermore, there are many other sources referring to the experiment that need to be considered. Table 6.1 lists all known uncertainties. Note that these are only estimations. Moreover, the Σ^+ selection is not included, since its uncertainty estimation would have required too much work in the course of a master's thesis. The sum in quadrature of these errors yields 8 %. To obtain the overall uncertainty, this value needs to be summed in quadrature with the result given by the comparison of the two methods:

$$\sigma_{\text{sys}} = \sqrt{(7\,\%)^2 + (8\,\%)^2} = 10.6\,\%$$

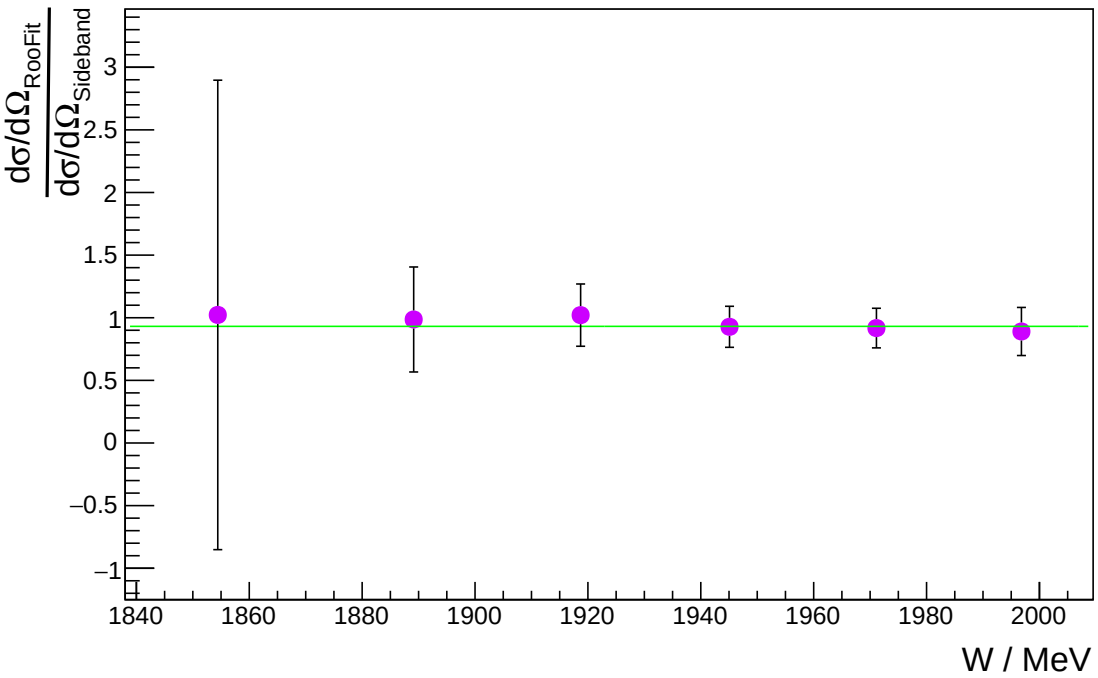

Figure 6.6: Ratio of the cross section determined with the RooFit method and the result obtained with the Sideband method. The green line is a linear fit to the data.

Source	% Error
Beam spot alignment	4.0
Photon flux	4.0
K^+ selection	2.0
SciFi efficiency	3.0
Target wall contribution	2.0
Track time selection	2.0
Target length	1.7
ToF wall efficiency	1.5
MOMO efficiency	1.0
Drift chamber efficiency	1.0
Beam energy calibration	1.0
Modelling of hardware triggers	1.0
π^0 identification	1.0
Forward track geometric selection	1.0
Summed in quadrature	8.0

Table 6.1: Estimated systematic uncertainties from different sources. Summed in quadrature, the overall uncertainty is 8 % [35].

In order to obtain an absolute estimation for the error, the differential cross section can be multiplied by the overall uncertainty of approximately 11 %, and plotted as a bar chart together with the cross section. This is done for both methods and can be seen in the Appendix D.

The contribution from $\Sigma(1385)$ also needs to be taken into account in the systematic uncertainty estimation. The overall systematic uncertainty for the cross section for $\gamma p \rightarrow K^+\Sigma(1385)$ has been estimated to 11.5 % [32]. However, this is not the only error that has to be regarded. As indicated in Section 6.4, the branching ratio for the decay $\Sigma(1385) \rightarrow (\Sigma\pi)^0$ is (11.7 ± 1.5) % [33]. The error of 1.5 %, given with this branching ratio, must be considered, too. Dividing this error by the branching ratio, one gets 12.8 %, which is non-negligible. The overall uncertainty has to be summed in quadrature with the error coming from the branching ratio. This sum must be scaled by the factor $(0.5 \cdot 0.117)$, analogously to the scaling of the cross section itself:

$$\sigma_{\text{sys, }\Sigma(1385)} = 0.5 \cdot 0.117 \cdot \sqrt{(11.5\,\%)^2 + (12.8\,\%)^2} = 1.0\,\%$$

In Fig. 6.7, one can see the scaled cross section with the corresponding statistical error bars and the systematic errors represented as a bar chart.

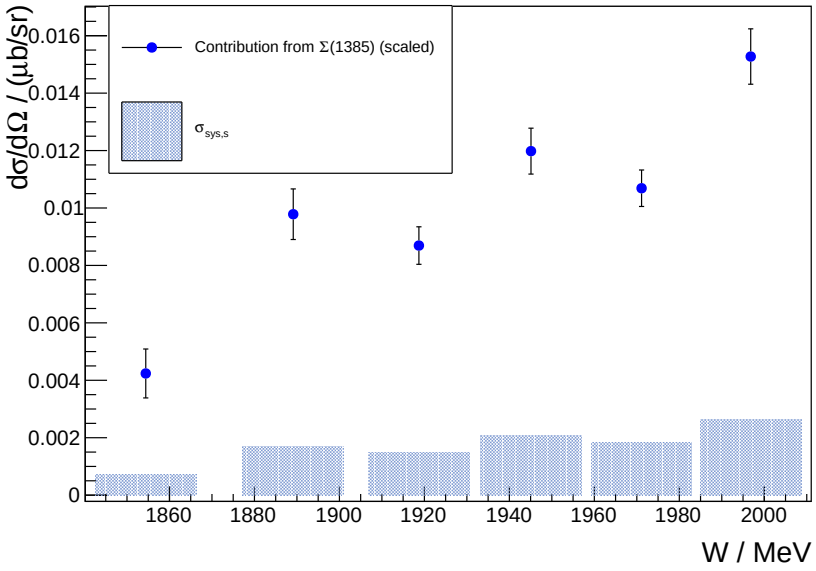

Figure 6.7: Scaled contribution from Σ(1385) and corresponding systematic uncertainties. For the creation of this diagram again the data from June 2018 provided by M. Jena were used [32].

6.5.1 Results for $\gamma p \to K^+\Lambda(1405)$

Until now, only the charged decay channel $\gamma p \to K^+\Sigma^+\pi^-$ was studied. In order to obtain the differential cross section for $\gamma p \to K^+\Lambda(1405)$, the results from Section 6.4 have to be multiplied by 3. It is possible to proceed like this because the branching ratio is equally $33.\overline{3}$ % for each channel. The overall systematic uncertainty for the reaction $\gamma p \to K^+\Lambda(1405)$ as a relative value, was estimated to be approximately 11 %. However, the absolute uncertainty also includes the contribution from Σ(1385) such, that the determined uncertainty of 1.0 % must be scaled with this contribution and added in quadrature to the 11 % which are scaled with the obtained cross section result for $\gamma p \to K^+\Lambda(1405)$. These results are shown in Fig. 6.8 for the RooFit method and Fig. 6.9 for the Sideband method.

Due to the subtraction of the contribution from Σ(1385), the first three data points appear to be negative, although the true value should be very close to zero and positive. The systematic and statistical errors of the second data point are not sufficiently large to explain the shift to negative values in both results. One reason for this shift could be that the fits made by the RooFit toolkit become worse for lower beam energies. In the Appendix A, we see that in the first distributions the background is indeed more dominant than the signal, since the beam energy is rather low. This is similar for the Sideband method. The corresponding plots are shown in Appendix B. It is clearly visible, that in the beginning, i.e., for a beam energy of $E_\gamma = 1\,339$ MeV or of $E_\gamma = 1\,412$ MeV, the background is much higher than the signal. With increasing beam energy, the signal becomes more visible. That means that the cross section values determined for lower beam energies, so the first three data points in the diagram, are maybe affected by this and thus less reliable. The fact that the estimation of the systematic uncertainty does not sufficiently account for the first data points could mean that the uncertainties are actually higher than estimated. In this thesis, the systematic uncertainty that rises from the determination of the Σ^+ mass selection was not considered due to the significant effort required to do this accurately. Other mass selections are taken from Table 6.1, which are general estimations. Ideally, the mass selection should have been varied to upper and lower values, and the corresponding results compared. Perhaps, the additional systematic error

from this part of the analysis could explain why the first three data point appear to be negative.

In general, a linear trend of the cross section is seen. However, the cross section value at almost 2 000 MeV is smaller than the previous one. Similar to low beam energies, there is no observable signal at very high beam energies.

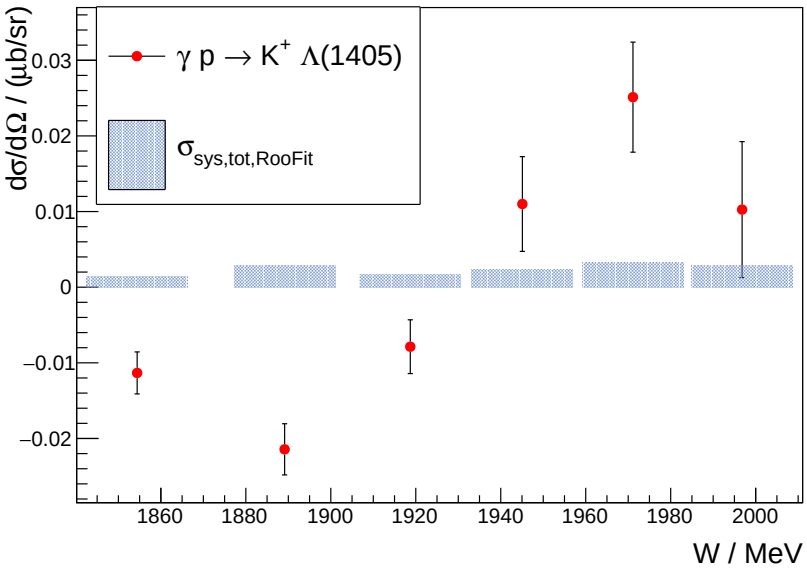

Figure 6.8: Differential cross section for $\gamma p \rightarrow K^{+}\Lambda(1405)$ for the RooFit method and corresponding systematic uncertainties.

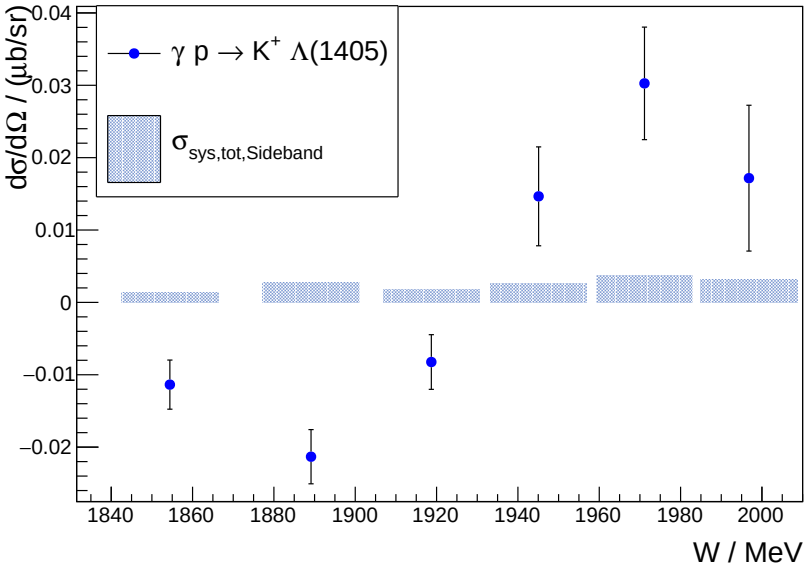

Figure 6.9: Differential cross section for $\gamma p \rightarrow K^{+}\Lambda(1405)$ for the Sideband method and corresponding systematic uncertainties.

The final results are depicted in one diagram, Fig. 6.10, and compared to the data from the CLAS Collaboration [20]. The cross section data taken from Ref. [20] were scaled so that the units of the cross section correspond to the results from this thesis. Moreover, it was scaled by 3 in order to represent the result for the entire process $\gamma p \to K^+\Lambda(1405)$.

In red, the differential cross section determined with the RooFit method is shown, in blue for the Sideband method and in green the results from CLAS. The cross sections from BGOOD have been determined in the center-of-mass range, $1\,850\,\text{MeV} < W < 2\,000\,\text{MeV}$, and go from approximately $-0.02\,\mu\text{b/sr}$ to $0.03\,\mu\text{b/sr}$ in a linear trend. These results were determined for angles in the range $0.9 < \cos\theta^{K^+}_{\text{CM}} < 1.0$. However, the cross section result presented by the CLAS Collaboration was determined for $\cos\theta^{K^+}_{\text{CM}} = 0.84$ and not for more forward angles. This means that both results do not allow for an exact comparison. The results from CLAS go up to 2 800 MeV while the BGOOD results follow a linear trend towards the treshold. This represents an important extension of the energy range from the CLAS measurement.

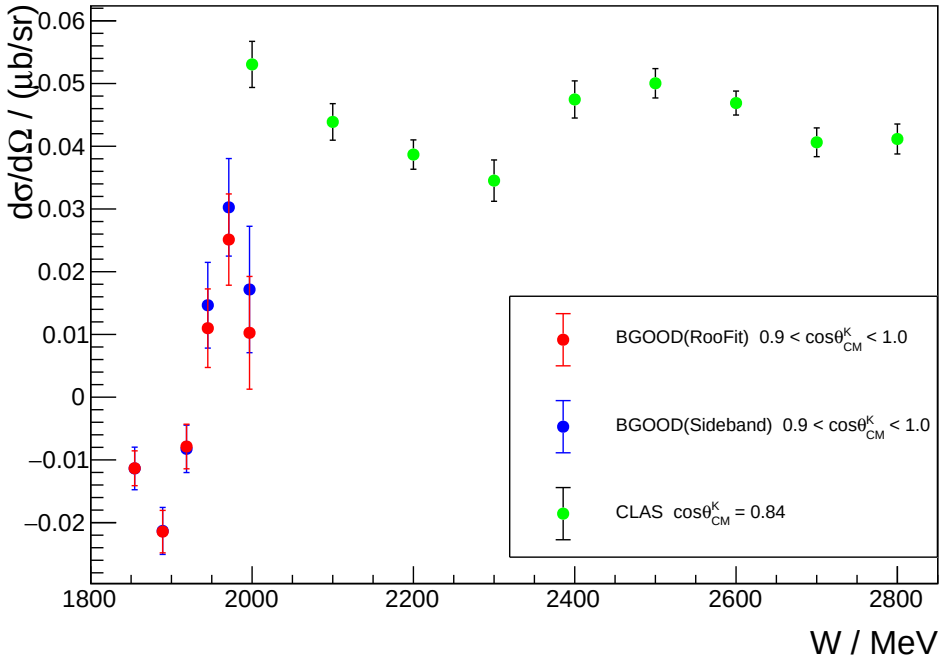

Figure 6.10: Differential cross section for $\gamma p \to K^+\Lambda(1405)$ in red and in blue, for the RooFit and Sideband method, respectively. The results are compared to the measurement of the photoproduction cross section from the CLAS Collaboration, shown in green. For the comparison, the data taken from [20] was scaled.

CHAPTER 7

Summary and outlook

In this thesis, the reaction $\gamma p \rightarrow K^+\Lambda(1405)$ was studied at the BGOOD experiment in Bonn. The $\Lambda(1405)$ resonance is subject to current research that goes beyond the Standard model of particle physics. Being a hyperon of strangeness $S = -1$ with quantum numbers $J^\pi = \frac{1}{2}^-$, it is lighter than the S_{11} baryon $N(1535)$ that has no strange quark. The common idea of three valence quarks does not fully explain this. The $\Lambda(1405)$ is most likely a more complex structure and can be described as a molecular state being composed of an antikaon $\bar{K}$, and a nucleon N.

The study of this dynamically generated resonance can be realized by experiments using meson photoproduction. This was already done by the CLAS Collaboration [16, 20]. The photoproduction line shapes of the three possible decay channels, $(\Sigma\pi)^0$, have been measured. Furthermore, the differential cross section for the $K^+\Lambda(1405)$ photoproduction has been determined for center-of-mass energies of 2 000 MeV and higher. Another measurement was conducted by G. Scheluchin at BGOOD, who investigated the neutral decay channel and determined the total photoproduction cross section [15, 21]. A good agreement with the results from the CLAS group was found having a better energy resolution.

This analysis work had the aim to extend the earlier measurements. The charged decay channel $\Sigma^+\pi^-$, was examined and the differential cross section for the $K^+\Lambda(1405)$ photoproduction was determined for angles $\cos\theta^{K^+}_{\mathrm{CM}} > 0.9$. The BGOOD experiment is perfectly designed for forward going particles so that very forward angles could be investigated.

The $\Lambda(1405)$ final state was reconstructed via the decay to $\Sigma^+\pi^- \rightarrow p\pi^0\pi^-$. The π^0 was identified in the central detector, the p and π^- via kinematic constraints. The yield was extracted using two different methods. The RooFit method applied template fits to the real data using background spectra from simulations. This includes among others the simulation for $\Lambda(1520)$. The Sideband method uses only background from misidentified π^+. No fits were made, but a sideband subtraction assured that in the end only the signal was left and could be integrated to obtain the yield. Especially, the missing information from the $\Lambda(1520)$ simulation can explain the deviation of the two methods.

At first, the result for the differential cross section for $\gamma p \rightarrow K^+\Sigma^+\pi^-$ was shown. There are two possible reactions with the same decay channel, $\Lambda(1405) \rightarrow \Sigma^+\pi^-$ and $\Sigma(1385) \rightarrow \Sigma^+\pi^-$. In order to obtain the $K^+\Lambda(1405)$ photoproduction cross section, the contribution from the $\Sigma(1385)$ had to be removed from the result. The already measured $K^+\Sigma(1385)$ cross section was scaled and subtracted. This was a non-negligible fraction of the entire photoproduction cross section.

The two methods for the yield extraction and several experimental uncertainties contributed to a total systematic uncertainty of 11 %. The subtraction of the $\Sigma(1385)$ part led to an overall systematic uncertainty of 1 %, which was included as an absolute error. The obtained uncertainties could not explain the shift of the first data points to negative values. More work on this or an improvement of the methods

for the yield extraction could solve this.

The final results were compared to the measurements from the CLAS Collaboration. It could be stated that the differential photoproduction cross section determined in this thesis extends the energy range from the CLAS result towards the threshold. This is the first time, that the differential cross section for the photoproduction of $K^+\Lambda(1405)$ could be measured for extremely forward angles and close to threshold. Such measurements are crucial in understanding the molecular nature of the $\Lambda(1405)$ baryon. Further studies with more data will be made at BGOOD. Moreover, measurements of the line shape over this region will also be performed at the BGOOD experiment.

APPENDIX A

Fits made with RooFit

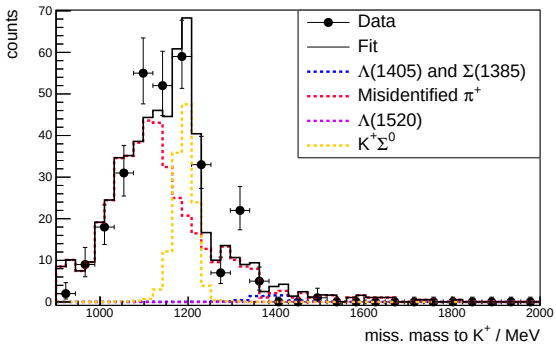

Figure A.1: Real and simulated data with fit using RooFit for $E_\gamma = 1\,339\,\text{MeV}$.

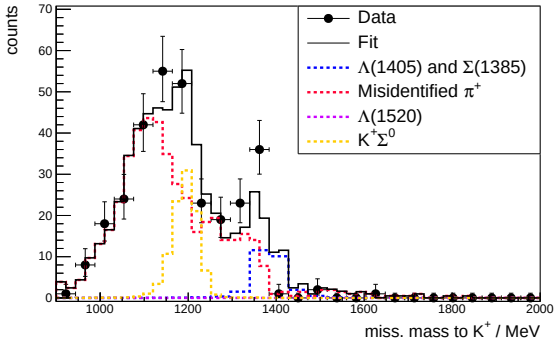

Figure A.2: Real and simulated data with fit using RooFit for $E_\gamma = 1\,411\,\text{MeV}$.

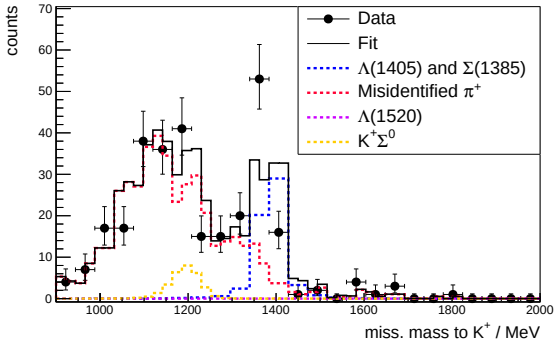

Figure A.3: Real and simulated data with fit using RooFit for $E_\gamma = 1\,475\,\text{MeV}$.

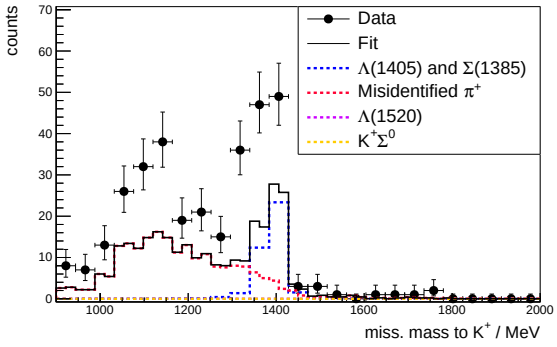

Figure A.4: Real and simulated data with fit using RooFit for $E_\gamma = 1\,529\,\text{MeV}$.

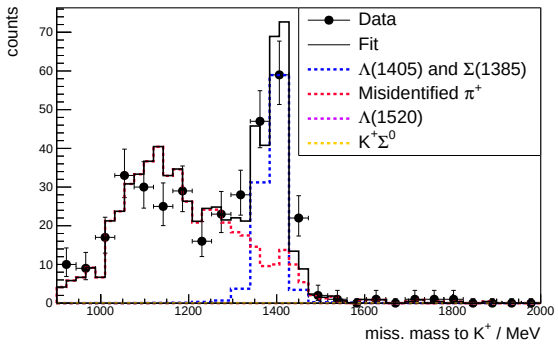

Figure A.5: Real and simulated data with fit using RooFit for $E_\gamma = 1\,583\,\text{MeV}$.

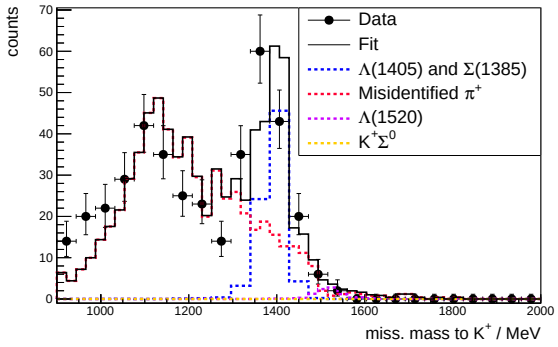

Figure A.6: Real and simulated data with fit using RooFit for $E_\gamma = 1\,638\,\text{MeV}$.

APPENDIX B

Plots from the Sideband method

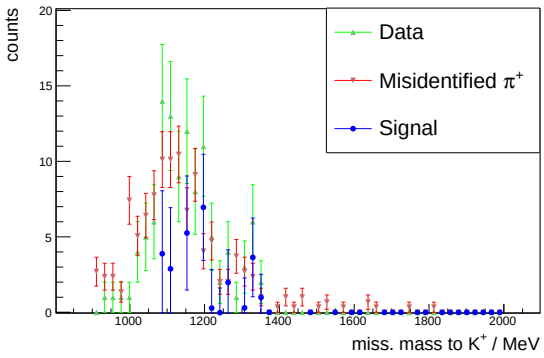

Figure B.1: Data, background from misidentified π^+ and signal using the Sideband method for E_γ = 1 339 MeV.

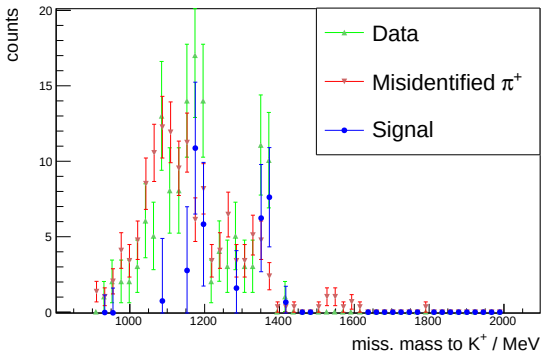

Figure B.2: Data, background from misidentified π^+ and signal using the Sideband method for E_γ = 1 412 MeV.

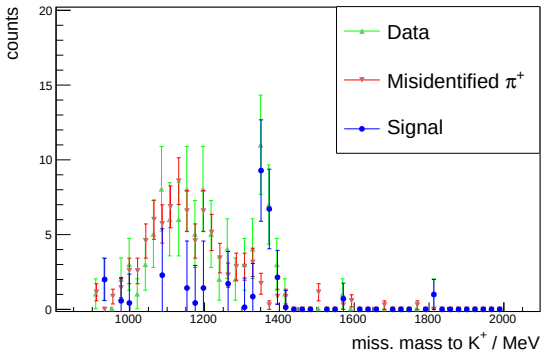

Figure B.3: Data, background from misidentified π^+ and signal using the Sideband method for E_γ = 1 475 MeV.

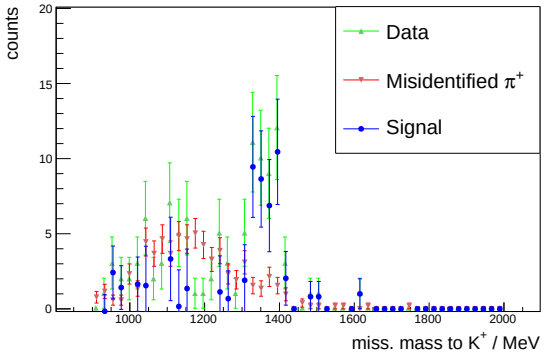

Figure B.4: Data, background from misidentified π^+ and signal using the Sideband method for E_γ = 1 529 MeV.

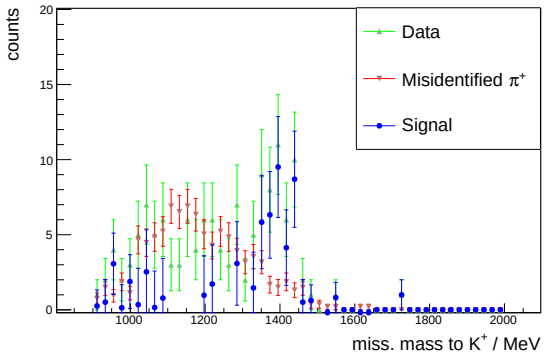

Figure B.5: Data, background from misidentified π^+ and signal using the Sideband method for $E_\gamma = 1\,583\,\text{MeV}$.

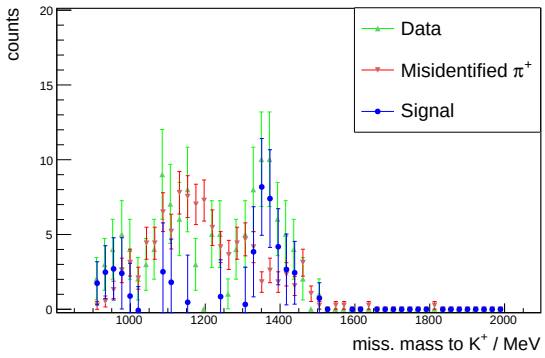

Figure B.6: Data, background from misidentified π^+ and signal using the Sideband method for $E_\gamma = 1\,638\,\text{MeV}$.

APPENDIX C

Differential cross section for $\gamma p \rightarrow K^{+}\Sigma(1385)$

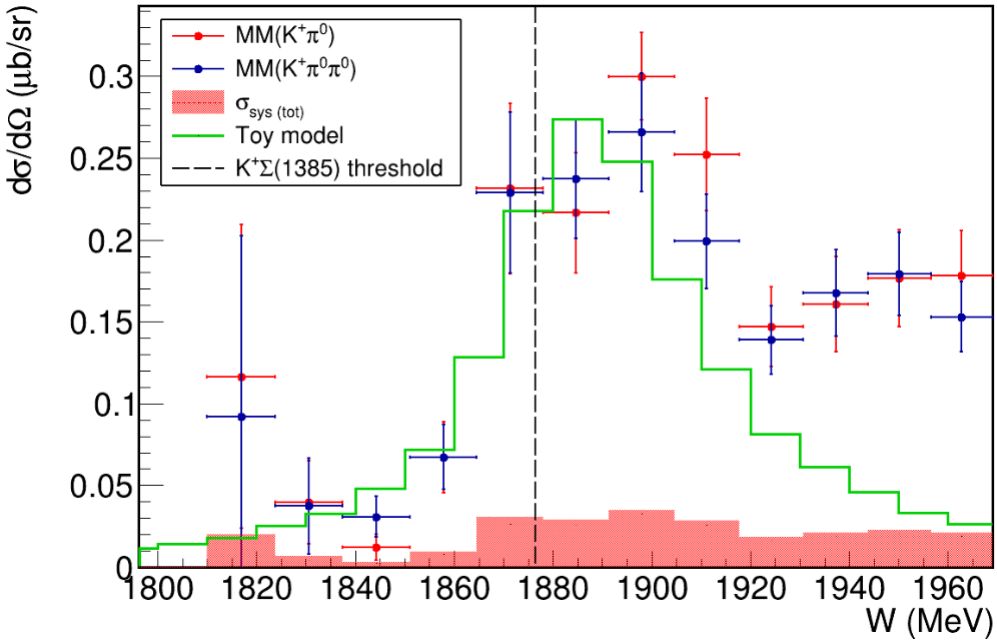

Figure C.1: Differential cross section for $\gamma p \rightarrow K^{+}\Sigma(1385)$ (2017 data) [32].

APPENDIX D

Cross section for $\gamma p \rightarrow K^+\Sigma^+\pi^-$

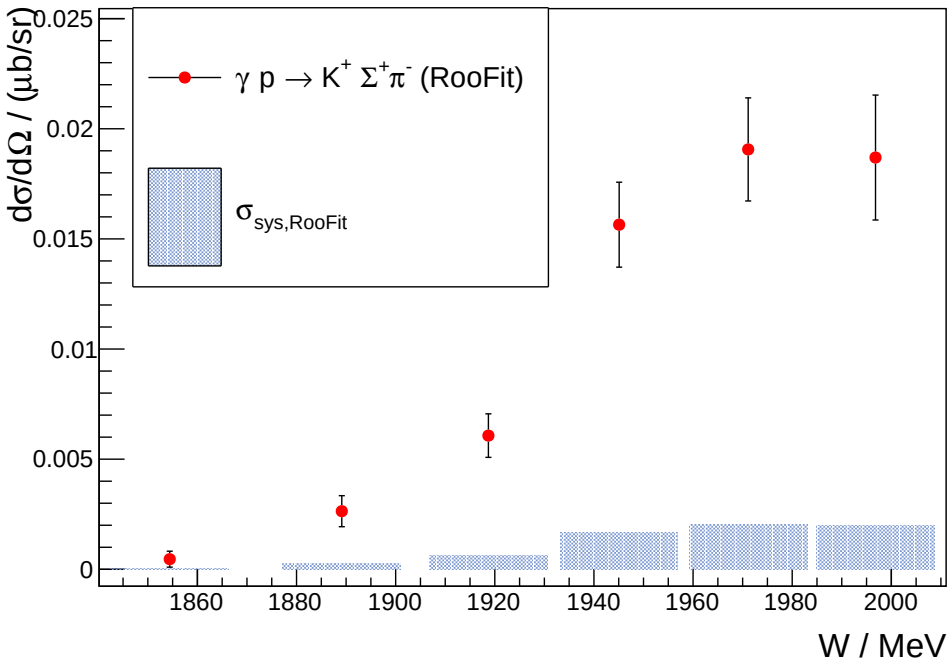

Figure D.1: Differential cross section for $\gamma p \rightarrow K^+\Sigma^+\pi^-$, determined with the RooFit method of extracting yield and corresponding systematic errors.

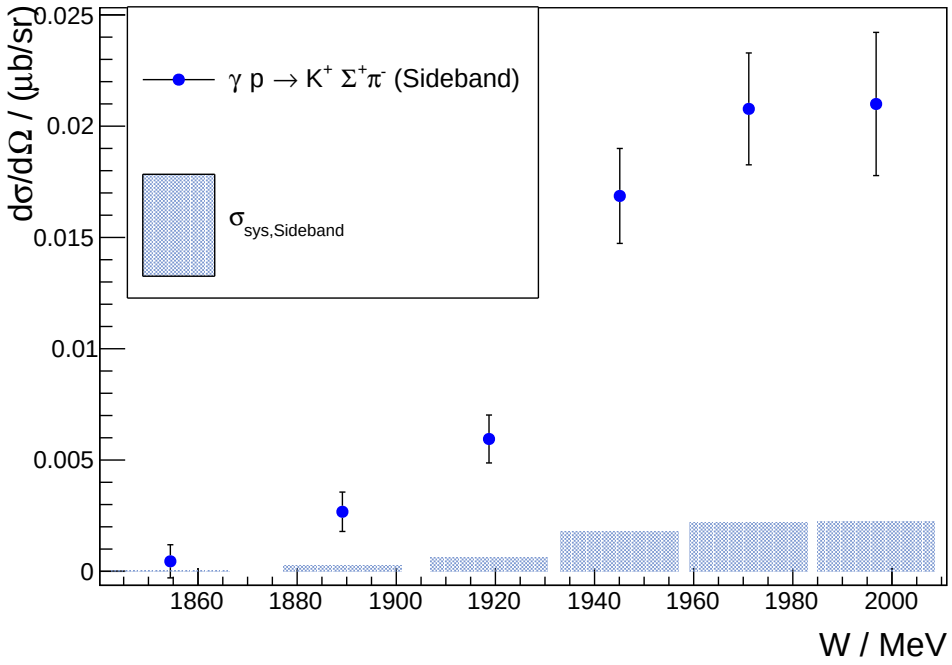

Figure D.2: Differential cross section for $\gamma p \to K^+\Sigma^+\pi^-$, determined with the Sideband method of extracting yield and corresponding systematic errors.

Bibliography

[1] D. Dominguez/CERN, 2015. https://home.cern/science/physics/standard-model.

[2] M. Gaillard et al., *The Standard Model of Particle Physics*, Reviews of Modern Physics **71** (1999) S96–S111.

[3] ATLAS Collaboration, *Observation of a new particle in the search for the Standard Model Higgs boson with the ATLAS detector at the LHC*, Physics Letters B **716** (2012) 1–29.

[4] U. Löring et al., *The light baryon spectrum in a relativistic quark model with instanton-induced quark forces II. The strange baryon spectrum*, Eur. Phys. J. A **10** (2001) 447–486.

[5] U. Thoma, *The search for missing baryon resonances*, AIP Conference Proceedings (2005).

[6] U. Löring et al., *The light baryon spectrum in a relativistic quark model with instanton-induced quark forces I. The non-strange baryon spectrum and ground-states*, Eur. Phys. J. A **10** (2001) 395.

[7] R. Jaffe, *Multiquark hadrons. I. Phenomenology of* $Q^2\overline{Q}^2$ *mesons*, Phys. Rev. D **15** (1977) 267–280.

[8] K. Hicks, *Pentaquarks: Introduction and review*, Acta Phys. Polon. B **35** (2004) 3039.

[9] L. Yan-Rui, *Pentaquark and Tetraquark States*, Progress in Particle and Nuclear Physics **107** (2019) 237–320.

[10] R. Dalitz and S. Tuan, *Possible Resonant State in Pion-Hyperon Scattering*, Phys. Rev. Lett. **2** (1959) 425–428.

[11] R. Dalitz and S. Tuan, *The phenomenological representation of scattering and reaction amplitudes*, Ann. Phys. **10** (1960) 307–351.

[12] Y. Nogami, *Possible existence of* $\bar{K}NN$ *bound states*, Phys. Lett. **7** (1963) 288–289.

[13] PDG, 2016. https://pdg.lbl.gov/2016/reviews/rpp2016-rev-lam-1405-pole-struct.pdf.

[14] R. Hemingway, *Production of* $\Lambda(1405)$ *in* $K^- p$ *reactions at 4.2 GeV/c*, Nucl. Phys. B **253** (1985) 742.

[15] G. Scheluchin, $\Lambda(1405)$ *photoproduction with the BGO-OD experiment*. Dissertation: Rheinische Friedrich-Wilhelms-Universität Bonn, (2019).

[16] K. Moriya et al., *Measurement of the* $\Sigma\pi$ *photoproduction line shapes near the* $\Lambda(1405)$, Phys. Rev. C **87** (2013) 35–206.

[17] D. Jido, *Chiral dynamics of the two* $\Lambda(1405)$ *states*, Nucl. Phys. A **725** (2003) 181.

[18] M. Mai and U. Meißner, *Constraints on the chiral unitary $\bar{K}N$ amplitude from $\pi\Sigma K^+$ photoproduction data*, Eur. Phys. J. A **51** (2015) 30.

[19] V. Bernard, N. Kaiser, and U. Meißner, *Chiral Dynamics in Nucleons and Nuclei*, International Journal of Modern Physics E **04** (1995) 193–344.

[20] K. Moriya et al., *Differential photoproduction cross sections of the* $\Sigma^0(1385)$*,* $\Lambda(1405)$*, and* $\Lambda(1520)$, Phys. Rev. C **88** (2013) 45–201.

[21] G. Scheluchin et al., *Photoproduction of* $K^+\Lambda(1405) \to K^+\pi^0\Sigma^0$ *extending to forward angles and low momentum transfer*, Phys. Lett. B **833** (2022) 137–375.

[22] E. Wang et al., *Role of a triangle singularity in the* $\gamma p \to K^+\Lambda(1405)$ *reaction*, Phys. Rev. C **95** (2017) 15–205.

[23] S. Alef et al., *The BGOOD experimental setup at ELSA*, Eur. Phys. J. A **56** (2020) 104.

[24] W. Hillert, *The Bonn electron stretcher accelerator ELSA: Past and future*, Eur. Phys. J. A **28S1** (2006) 139.

[25] W. Hillert et al., *Beam and spin dynamics in the fast ramping storage ring ELSA: Concepts and measures to increase beam energy, current and polarization*, EPJ Web Conf. **134** (2017) 05002.

[26] F. Messi, *The Tagging System of the BGO-OD experiment*. Dissertation: Rheinische Friedrich-Wilhelms-Universität Bonn, (2015).

[27] K. Kohl, *Measurement of the* $\gamma n \to K^0\Sigma^0$ *photoproduction at the BGOOD experiment and the relation to possible pentaquark states*. Dissertation: Rheinische Friedrich-Wilhelms-Universität Bonn, (2022).

[28] G. Scheluchin, *Meson photoproduction on the proton using the BGO-OD detector complemented by a new Scintillating Ring (SciRi),*. Master's thesis: Rheinische Friedrich-Wilhelms-Universität Bonn, (2015).

[29] O. Freyermuth, *Studies of* ω *Photoproduction off Proton at the BGO-OD Experiment*. Dissertation: Rheinische Friedrich-Wilhelms-Universität Bonn, (2017).

[30] R. Brun, *ROOT: an object oriented data analysis framework*, 1997. https://root.cern.ch.

[31] W. Verkerke and D. Kirkby, *The RooFit toolkit for data modeling*, 2003. physics/0306116.

[32] M. Jena, $\Sigma(1385)$ *photoproduction at the BGO-OD experiment*. Master's thesis: Rheinische Friedrich-Wilhelms-Universität Bonn, (2024). Note: The data from June 2018 was provided within a personal discussion.

[33] PDG, 2018. https://pdg.lbl.gov/2018/tables/rpp2018-tab-baryons-Sigma.pdf.

[34] PDG, 2002. https://pdg.lbl.gov/2002/clebrpp.pdf.

[35] S. Alef et al., $K^+\Lambda$ *photoproduction at forward angles and low momentum transfer*, Eur. Phys. J. A **57** (2021) 80.

List of Figures

1.1 The Standard Model of particle physics: subatomic particles [1]. 1

2.1 The calculated positive and negative parity Λ-resonance spectrum. The quantum numbers of the resonances are displayed on the x-axis, alongside their masses on the y-axis. The blue lines show the predicted states by theory, while the red lines indicate the measured states with their uncertainties delineated by yellow boxes [4]. 3
2.2 A pentaquark shown as a hadronic molecule of a meson and a baryon [1]. 4
2.3 Invariant mass distributions (or line shapes) of the final states, $(\Sigma\pi)^0$, of the Λ(1405) photoproduction. The $(\Sigma\pi)^0$ and $\bar{K}N$ thresholds as well as the Λ(1405) mass are marked by the vertical dashed lines. The results were obtained by the CLAS Collaboration [16]. 5
2.4 Two processes of Λ(1405) photoproduction [21]. 6
2.5 Total cross section for $\gamma p \to K^+\Lambda(1405)$ [21]. The black squares are the BGOOD data, the red circles are the data from the CLAS Collaboration. The systematic uncertainties are shown by the grey bars on the abscissa. The curves are the results of the model of Wang et al. [22]. 7

3.1 The Electrom Stretcher Accelerator (ELSA) facility with the LINAC 2, the booster synchrotron, the stretcher ring and the experiments [23]. 9
3.2 Overview of the BGOOD experiment showing the different components of the detector [23]. 10
3.3 The photon tagger along with its working principle [23]. 11
3.4 The central detector featuring the BGO Rugby ball calorimeter as its primary component among other modules [27]. 12
3.5 Overview of the forward spectrometer [27]. 13
3.6 **(a)** Identification of the positively charged particles π^+, K^+ and p from top to bottom in the forward spectrometer [23]. **(b)** The same particles classified by their masses calculated using momentum and β [23]. 14

4.1 Photoproduction of the Λ(1405) resonance in a t-channel exchange. Time goes from left to right [16]. 15
4.2 Decay scheme for the $K^+\Lambda(1405)$ photoproduction focusing on one specific charged channel: $\Lambda(1405) \to \Sigma^+\pi^-$. 16
4.3 Invariant mass distribution in the forward spectrometer used to determine the value for the kaon mass selection. The vertical dashed lines indicate the 2σ range around the kaon mass. 17
4.4 Invariant mass distribution of photon pairs used to determine the value for the pion mass selection. The vertical dashed lines indicate the 2σ range around the pion mass. 17

4.5 Sketch of the particle tracks and track angles. For simplicity, not all of the particles contributing to the reaction are shown. The Λ(1405) track is marked in green. It decays into a π^-, shown in orange and a Σ^+, shown in violet. The proton, marked in blue, is one of the final particles from the Σ^+. The angle between the proton and the Λ(1405) track is ϵ_1. The angle between the π^- and the Λ(1405) track is ϵ_2. 19
4.6 $\pi^-\pi^0 p$ invariant mass distribution for the case of a "correct π^-/p assignment". 20
4.7 $\pi^-\pi^0 p$ invariant mass distribution for the case of a "wrong π^-/p assignment". 20
4.8 Missing mass to $K^+\pi^-$ versus πp invariant mass. 21

5.1 Photon beam energy versus the missing mass to the K^+ for real data from June 2018. . 23
5.2 Missing mass to K^+, for the y bin range 57 − 59 and for a beam energy range of 1 755 MeV − 1 810 MeV, with angles $\cos\theta^{K^+}_{\mathrm{CM}} > 0.9$. 24
5.3 RooFit for E_γ = 1 583 MeV. Data points are shown as black circles, the full fit as a black solid line. Background channels are depicted as colored dashed lines. The main contribution comes from π^+ misidentified as K^+ (red dashed line). 25
5.4 Data, background and signal distribution for E_γ = 1 583 MeV. The background from the misidentified π^+ was scaled such, that it describes the green data. Afterwards, it is subtracted from the data, the remaining signal is shown in blue. 26
5.5 Yield for RooFit method in red and Sideband method in blue. 27

6.1 Detection efficiency in dependence of the photon beam energy. Three bins are grouped together. 30
6.2 Differential cross sections for $\gamma p \to K^+\Sigma^+\pi^-$. In red, RooFit method for yield extraction, in blue, Sideband method. 31
6.3 Differential cross section for $\gamma p \to K^+\Sigma(1385)$ in yellow and the scaled cross section in blue where $\Sigma(1385) \to \Sigma^+\pi^-$ is the relevant decay channel. To obtain the blue cross section result, the yellow cross section was scaled by $(0.117 \cdot 0.5)$. The error bars are too small to be seen. The figure was created using data from June 2018 provided by M. Jena during his master's thesis [32]. 32
6.4 In pink: differential cross section for $\gamma p \to K^+\Sigma^+\pi^-$, determined with the RooFit method. This is the result before the subtraction of the Σ(1385) contribution. In red is shown the result after the subtraction. 33
6.5 In pink: differential cross section for $\gamma p \to K^+\Sigma^+\pi^-$, determined with the Sideband method. This is the result before the subtraction of the Σ(1385) contribution. In blue is shown the result after the subtraction. 33
6.6 Ratio of the cross section determined with the RooFit method and the result obtained with the Sideband method. The green line is a linear fit to the data. 34
6.7 Scaled contribution from Σ(1385) and corresponding systematic uncertainties. For the creation of this diagram again the data from June 2018 provided by M. Jena were used [32]. 36
6.8 Differential cross section for $\gamma p \to K^+\Lambda(1405)$ for the RooFit method and corresponding systematic uncertainties. 37
6.9 Differential cross section for $\gamma p \to K^+\Lambda(1405)$ for the Sideband method and corresponding systematic uncertainties. 37
6.10 Differential cross section for $\gamma p \to K^+\Lambda(1405)$ in red and in blue, for the RooFit and Sideband method, respectively. The results are compared to the measurement of the photoproduction cross section from the CLAS Collaboration, shown in green. For the comparison, the data taken from [20] was scaled. 38

A.1 Real and simulated data with fit using RooFit for $E_\gamma = 1\,339$ MeV. 41
A.2 Real and simulated data with fit using RooFit for $E_\gamma = 1\,411$ MeV. 41
A.3 Real and simulated data with fit using RooFit for $E_\gamma = 1\,475$ MeV. 41
A.4 Real and simulated data with fit using RooFit for $E_\gamma = 1\,529$ MeV. 41
A.5 Real and simulated data with fit using RooFit for $E_\gamma = 1\,583$ MeV. 42
A.6 Real and simulated data with fit using RooFit for $E_\gamma = 1\,638$ MeV. 42

B.1 Data, background from misidentified π^+ and signal using the Sideband method for $E_\gamma = 1\,339$ MeV. 43
B.2 Data, background from misidentified π^+ and signal using the Sideband method for $E_\gamma = 1\,412$ MeV. 43
B.3 Data, background from misidentified π^+ and signal using the Sideband method for $E_\gamma = 1\,475$ MeV. 43
B.4 Data, background from misidentified π^+ and signal using the Sideband method for $E_\gamma = 1\,529$ MeV. 43
B.5 Data, background from misidentified π^+ and signal using the Sideband method for $E_\gamma = 1\,583$ MeV. 44
B.6 Data, background from misidentified π^+ and signal using the Sideband method for $E_\gamma = 1\,638$ MeV. 44

C.1 Differential cross section for $\gamma p \to K^+\Sigma(1385)$ (2017 data) [32]. 45

D.1 Differential cross section for $\gamma p \to K^+\Sigma^+\pi^-$, determined with the RooFit method of extracting yield and corresponding systematic errors. 47
D.2 Differential cross section for $\gamma p \to K^+\Sigma^+\pi^-$, determined with the Sideband method of extracting yield and corresponding systematic errors. 48

List of Tables

6.1 Estimated systematic uncertainties from different sources. Summed in quadrature, the overall uncertainty is 8 % [35]. 35